Representing the geometrical complexity of liners and boundaries in low-order modeling for thermoacoustic instabilities

C. Laurent, A. Badhe, Franck Nicoud

Representing the geometrical complexity of liners and boundaries in low-order modeling for thermoacoustic instabilities

C. Laurent [a,*], A. Badhe [a], F. Nicoud [b]

[a] CERFACS, 42 Avenue Gaspard Coriolis, 31057 Toulouse Cedex 1, France
[b] IMAG, Univ. Montpellier, CNRS, Montpellier, France

ARTICLE INFO

Article history:
Received 22 July 2020
Received in revised form 15 November 2020
Accepted 9 December 2020
Available online 28 December 2020

Keywords:
Thermoacoustic instabilities
Low Order Model
Modal expansion
Acoustic liner
Boundary conditions
State-space

ABSTRACT

This work introduces a novel method to represent the topological complexity of liners and boundaries in Low Order Models for thermoacoustic instabilities, under the assumption of zero-Mach number flow. In typical industrial combustion devices, the difficulty to model these elements is twofold: (1) they are characterized by complex-valued Rayleigh conductivities or acoustic impedances, and (2) they consist of large, curved panels whose geometries have first-order effect on the combustor thermoacoustic stability. To deal with the first point, the present approach makes use of a frame modal expansion recently introduced by Laurent et al. (2019) [41], which is a generalization of the classical rigid-wall Galerkin expansion, intended to deal with non-trivial boundary conditions. The core of this work lies in the second difficulty: complex-shaped liners and boundaries are modeled as two-dimensional manifolds, for which a specific set of curvilinear governing equations is derived. The inclusion of acoustic impedance or Rayleigh conductivity into these equations enforces the proper conservation equations at the frontiers of the adjacent volumes. Surface modal projections are then introduced to expand acoustic variables onto an orthogonal basis of modes solutions of a curvilinear Helmholtz eigenproblem. The resulting dynamical system is embedded into a state-space framework to build acoustic networks. A first non-reacting canonical test case, consisting of a multi-perforated liner in a cylindrical geometry is studied to assess the convergence and precision of the method. The ability of the approach to deal with realistic reacting cases is then illustrated by modeling the partially reflecting outlet of a multi-sector annular combustor typical of industrial gas turbines. This methodology enables the inclusion of liners and other boundaries of arbitrary geometrical complexity in modal projection-based thermoacoustic Low Order Models.

1. Introduction

Thermoacoustic instabilities, which result from a constructive interaction between acoustic waves and a heat source placed in a confined space, have been a major issue for the design of gas turbines [1] and rocket engines [2,3] during the past decades. Developing the future generations of low-emissions combustion-based energy production devices requires a thorough understanding of this phenomenon, in order to predict and ideally avoid it at the design level. Although significant

* Corresponding author.
E-mail address: laurent@cerfacs.fr (C. Laurent).

progress was accomplished in the comprehension of thermoacoustic instabilities since the first studies of Lord Rayleigh [4], this question still remains a major scientific challenge. Most research efforts have focused on designing experimental facilities typical of the industrial configurations of interest [5], as well as developing increasingly accurate and efficient numerical tools. Since thermoacoustic instabilities involve intricate interactions between multiple physical phenomena, their study with brute force high-order numerical methods such as Large Eddy Simulation (LES) [6,7] proved to be extremely costly, which drove the success of Low Order Models (LOMs).

Usual thermoacoustic LOMs are physics-based rather than data-based, and therefore rely on a set of simplifying assumptions. The first hypothesis consists in separating the acoustics and the flame dynamics: the former are solution of the frequency domain Helmholtz equation in which the latter are embedded as a source term represented by a Flame Transfer Function (FTF) [8]. This strategy led to the development of Finite Element Method (FEM) solvers for the Helmholtz equation, able to compute acoustic eigenmodes in elaborate geometries featuring active flames and complex impedance boundary conditions [9–13]. State-of-the-art FEM Helmholtz solvers also have the ability to account for multi-perforated liners located within the combustor [14–16], or scattering matrices [17]. Although the cost associated with FEM Helmholtz solvers is several orders of magnitude lower than that of full-order methods, they still require up to millions of Degrees of Freedom (DoF), which is prohibitive for computationally intensive applications such as multi-dimensional parametric studies, uncertainty quantification [18], or robust design. To further reduce the computational burden, additional simplifications are usually considered, for example by assimilating long ducts to purely one-dimensional elements, by replacing a gas turbine combustor with an idealized infinitely thin annulus [19], or by separating the liners and other non-trivial boundaries from the rest of the system. These elements of different dimensions and natures can then be combined with other components to form a heterogeneous acoustic network (Fig. 1). This strategy led to the development of a number of well-established tools, among which the Tax LOM [20,21], LOTAN [22,23], or the open-source OSCILOS [24–26]. A key characteristic of any thermoacoustic LOM lies in its ability to account for the elements found in industrial combustors that have first-order effect on their stability. Those for instance include multi-perforated liners, and chocked inlet or outlet, that may in addition be linked to a turbine or a compressor. The representation of complex-valued impedance boundaries at the inlet or outlet of idealized gas turbine annular combustors has been the focus of numerous low-order computational studies [22,23,25,27]. In this matter, the Riemann invariants A^+ and A^- combined to a basis of analytical Galerkin modes are usually utilized to decompose the three-dimensional acoustic fields. The modeling of multi-perforated liners, located either on internal walls or between a combustion chamber and its casing, has also been the subject of some attention. In one of the earliest attempt in this direction, Namba and Fukushige [28] replaced the lined walls of a straight duct by an equivalent distribution of monopole acoustic sources, and made use of the associated Green's function to resolve the acoustic problem. A similar approach was used by Sun et al. [29] to quantify the effect of liners on turbofan noise, and by Zhang et al. [30] to assess the damping of thermoacoustic instabilities by a drum-like silencer. In a different fashion, Cardenas-Miranda and Polifke [31] employed an integral mode matching method [32] to model a resonator ring and the damping it induces on the thermoacoustic modes of an idealized cylindrical rocket thrust chamber. Recently, Zhang et al. [33] used an expansion of the acoustic variables onto the Riemann invariants and a Galerkin basis of radial modes to build a network comprising lined walls; strategies to control the instabilities of an idealized annular combustor were then proposed.

Despite indisputable improvements, the inclusion of realistic liners and other boundaries in thermoacoustic LOMs still faces a twofold difficulty. On one hand, such boundaries are characterized by complex-valued impedances or Rayleigh conductivities. On the other hand, they often consist of large and curved panels, whose complex geometry may have a first-order effect on the system stability. To deal with the former point, most LOMs previously mentioned rely on a wave-based approach where the acoustic variables are decomposed onto the Riemann invariants. This strategy, however, is only applicable to idealized geometries, such as straight ducts and perfectly annular or cylindrical cavities. Bethke et al. [34] showed that Galerkin projection LOMs were not subjected to this limitation, by expanding the acoustic pressure on a modal basis obtained in a preliminary step thanks to a FEM Helmholtz solver. Conversely, their approach cannot address the former difficulty, as it is unable to represent complex-valued impedance boundary conditions. In the classical modal expansion introduced by Morse [35] and later popularized by Culick et al. [36–39], the acoustic pressure is indeed expressed as a summation of known acoustic modes satisfying *rigid-wall* conditions over the boundaries of the domain, and such expansion is therefore unable to accurately represent non-rigid-wall frontiers. This limitation was somewhat relaxed by Ghirado et al. [40], who formulated the Galerkin projection in an annular combustor with a complex inlet impedance as a perturbation problem of that with rigid-wall boundaries. This technique is however only applicable to cases where the impedance value slightly deviates from a homogeneous Neumann boundary condition. Thus, the combination of the two difficulties mentioned above greatly restrict the quantitative applicability to industrial combustors of existing thermoacoustic LOMs, which are rather limited to the qualitative analysis of idealized systems.

The main contribution of this work is the derivation of a low-order approach intended to accurately model surfaces of arbitrarily complex shape, where any complex-valued impedance or conductivity is prescribed. To deal with the latter point, it relies on a novel class of modal expansion proposed by Laurent et al. [41] to overcome the restrictions of the classical Galerkin expansion. In this view, the pressure is expanded onto an over-complete family of acoustic modes called a *frame*, which gathers rigid-wall ($u' = 0$) and pressure-release ($p' = 0$) eigenmodes. It was proved that this frame expansion has the potential to accurately satisfy any prescribed boundary condition. Although providing significant improvement in comparison with the classical rigid-wall modal expansion, the frame method does not directly address the geometrical complexity of boundaries encountered in realistic combustion systems, which is therefore the principal focus of the present work. To do so,

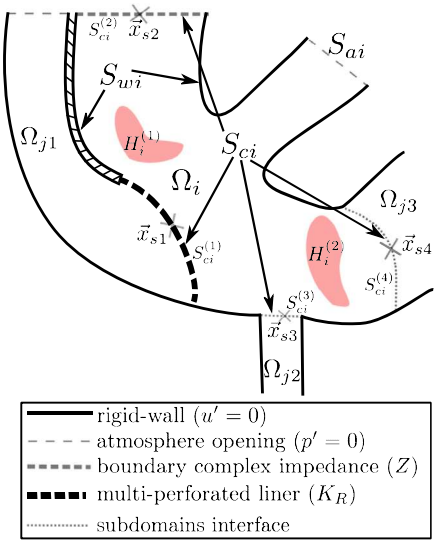

Fig. 1. Schematic of an acoustic network. The system is divided into a set of simpler subsystems comprising volume subdomains (Ω_i, Ω_{j1}, Ω_{j2}), heat sources ($H_i^{(1)}$, $H_i^{(2)}$), and subdomains complex boundaries ($S_{ci}^{(1)}$, $S_{ci}^{(2)}$, $S_{ci}^{(3)}$, $S_{ci}^{(4)}$). The subdomain Ω_i frontier is split into its rigid-wall boundary S_{wi}, its boundary opened to the atmosphere S_{ai}, and its connection boundary S_{ci}. This latter consists of $M_S = 4$ subsurfaces including simple interfaces ($S_{ci}^{(3)}$, $S_{ci}^{(4)}$), multi-perforated liners ($S_{ci}^{(1)}$), complex outlet impedance ($S_{ci}^{(2)}$), and any other type of boundary that is neither a rigid-wall nor an opening to the atmosphere. The center of each subsurface $S_{ci}^{(m)}$ is located at $\vec{x}_{sm}$.

the proposed approach is strongly inspired by the Acoustoelastic method [42–44], where acoustics in cavities are coupled with thin vibrating membranes. Complex-shaped liners and other boundaries are modeled as two-dimensional manifolds where acoustic variables are governed by a specific set of curvilinear equations. Complex-valued impedances or conductivities are embedded into this set to enforce the appropriate conservation relations across the boundary. A dynamical system governing the acoustics in the complex-shaped manifold is then derived by performing surface modal projections onto an orthogonal basis formed from solutions of a curvilinear Helmholtz eigenproblem. This dynamical system is reformulated into a state-space realization that can be implanted in any acoustic network. The paper is structured as follows: Section 2 first briefly recalls the state-space formalism as well as the frame expansion; the modeling of complex boundaries thanks to surface modal projections is then introduced. In Section 3 the method is validated on a canonical non-reacting case consisting of an annular multi-perforated liner within a cylindrical geometry. Finally, in Section 4, the potential of the method to handle complex industrial configurations is assessed by modeling the conical partially reflecting outlet of a multi-sector combustor comprising flames.

2. Derivation of a low order model for complex-shape boundaries

Low-order modeling of termoacoustic instabilities in complex geometries often relies on a *divide and conquer* strategy to build acoustic networks:

1. The combustor is split into a set of smaller subsystems, as illustrated in Fig. 1, where the thermoacoustic problem is easier to solve.
2. Governing equations for each individual subsystems are formulated.
3. Subsystems are recombined to assemble a set of coupled equations that is a low-order approximation of the full thermoacoustic problem.

This section first details the implementation of these steps in the present LOM, by briefly recalling the state-space formalism and the frame modal expansion. It then introduces the core of this work which is the derivation of a low-order approach to account for topologically complex boundary conditions in this framework.

2.1. Acoustic network and state-space representation

The decomposition of a combustor into a network of simpler subsystems is shown in Fig. 1. These subsystems can be sorted in distinct classes: volume subdomains (*e.g.* Ω_i), complex subdomains boundaries (*e.g.* $S_{ci}^{(1)}$ to $S_{ci}^{(4)}$, located on the frontier of Ω_i), and heat sources (*e.g.* $H_i^{(1)}$ and $H_i^{(2)}$, contained within Ω_i). Equations governing the intrinsic dynamics of each individual subsystem, as well as the coupling that may exist between distinct subsystems need to be formulated. The

state-space formalism, largely adopted by the thermoacoustics community [20,41,45–50], is an efficient way to achieve this step. The state-space representation for any subsystem (i) in the network writes:

$$\begin{cases} \dot{\mathbf{X}}^{(i)}(t) = \mathbf{A}^{(i)}\,\mathbf{X}^{(i)}(t) + \mathbf{B}^{(i)}\,\mathbf{U}^{(i)}(t) \\ \mathbf{Y}^{(i)}(t) = \mathbf{C}^{(i)}\,\mathbf{X}^{(i)}(t) + \mathbf{D}^{(i)}\,\mathbf{U}^{(i)}(t) \end{cases} \tag{1}$$

where $\mathbf{X}^{(i)}$ is the state vector (size $n \times 1$), $\mathbf{A}^{(i)}$ is the dynamics matrix ($n \times n$), $\mathbf{U}^{(i)}$ is the input vector ($k \times 1$), $\mathbf{B}^{(i)}$ is the input matrix ($n \times k$), $\mathbf{Y}^{(i)}$ is the output vector ($l \times 1$), $\mathbf{C}^{(i)}$ is the output matrix ($l \times n$), and $\mathbf{D}^{(i)}$ is the action matrix ($l \times k$). Dynamical variables of interest in the subsystem (i) are stored in the state-vector $\mathbf{X}^{(i)}$. The input matrix $\mathbf{B}^{(i)}$ and the input vector $\mathbf{U}^{(i)}$ are used to compute the forcing imposed onto the subsystem (i) by other components of the network. Therefore, the first line of Eq. (1) is a dynamical system governing the temporal evolution of the state-variables in the subsystem (i), under the forcing from the rest of the network. Conversely, the second line of Eq. (1) is used to compute the forcing applied by the subsystem (i) onto other elements in the network. In all the cases considered in the following, the action matrix $\mathbf{D}^{(i)}$ is zero and will therefore be ignored.

State-space representations of every subsystems in the network are then assembled by applying recursively the Redheffer product [51], which essentially consists in relating the input and output vectors of subsystems that are connected. This operation is detailed in [41] and is recalled in Supplemental Material A. Equivalent results can also be obtained through an analogous procedure named state-space interconnect [20]. The assembling step yields the state-space representation of the complete thermoacoustic system:

$$\dot{\mathbf{X}}(t) = \mathbf{A}\,\mathbf{X}(t) + \mathbf{B}\,\mathbf{U}(t) \tag{2}$$

where the input vector $\mathbf{U}$ and matrix $\mathbf{B}$ represent an external forcing. This equation can be integrated in time, or the eigenvalues and eigenvectors of the dynamics matrix $\mathbf{A}$ can be computed to obtain the thermoacoustic eigenmodes, with their respective eigen-frequencies and growth rates. This work focuses on the latter approach. The challenge now consists in deriving a state-space representation similar to Eq. (1) for every type of subsystems in the network. Section 2.2 recalls the state-space realization for a volume subdomain Ω_i, and Sec. 2.3 introduces the derivation of the state-space representation for a subdomain complex boundary $S_{ci}^{(m)}$.

2.2. Frame modal expansion for subdomain acoustics

Let us consider a volume subdomain Ω_i such as the one in Fig. 1. In the most general case, its boundary $\partial\Omega_i$ can be decomposed as: $\partial\Omega_i = S_{wi} \cup S_{ai} \cup S_{ci}$, where S_{wi} is a rigid-wall ($u'_s = \vec{u}'.\vec{n}_s = 0$), S_{ai} is opened to the atmosphere ($p' = 0$), and S_{ci} is a connection boundary containing any complex frontier that is neither rigid-wall nor pressure release. More precisely, S_{ci} contains boundaries with the exterior characterized by a finite impedance Z (*e.g.* chocked inlet or outlet), boundaries between two subdomains with a finite Rayleigh conductivity K_R (*e.g.* multi-perforated liner), and simple subdomains interfaces (which can also be characterized by a conductivity $K_R = \infty$). The boundary S_{ci} is further split into M_S subsurfaces $S_{ci}^{(m)}$, as depicted in Fig. 1.

In classical linear thermoacoustics under the zero Mach assumption, the Fourier transform of the acoustic pressure in the subdomain Ω_i is solution of the following frequency-domain inhomogeneous Helmholtz equation:

$$\begin{cases} c_0^2 \nabla^2 \hat{p}(\vec{x},\omega) - j\omega\delta\hat{p}(\vec{x},\omega) + \omega^2 \hat{p}(\vec{x},\omega) = \hat{h}(\vec{x},\omega) \;\text{ for }\; \vec{x} \in \Omega_i \\ \nabla_s \hat{p} = 0 \;\text{ for }\; \vec{x}_s \in S_{wi} \;\;,\;\; \hat{p} = 0 \;\text{ for }\; \vec{x}_s \in S_{ai} \\ \nabla_s \hat{p} = \hat{f}(\vec{x}_s,\omega) \;\text{ or }\; \hat{p} = \hat{g}(\vec{x}_s,\omega) \;\text{ for }\; \vec{x}_s \in S_{ci} \end{cases} \tag{3}$$

where δ is an acoustic loss coefficient, $\hat{h}(\vec{x},\omega)$ is a volume source term, and $\nabla_s \hat{p} = \vec{\nabla}\hat{p}.\vec{n}_s$ is the acoustic surface flux, $\vec{n}_s$ being the outwards-pointing surface normal vector at the point $\vec{x}_s$. Note the homogeneous Neumann condition on S_{wi} and the homogeneous Dirichlet condition on S_{ai}. The condition on the connection boundary S_{ci} is inhomogeneous of either Neumann or Dirichlet type, and $\hat{f}(\vec{x}_s,\omega)$ and $\hat{g}(\vec{x}_s,\omega)$ are a surface source terms imposed onto Ω_i by the adjacent subsystems. In Eq. (3), even though the mean sound speed c_0 is assumed uniform for clarity, this hypothesis is not necessary and the reasoning can be extended to inhomogeneous mean fields. The term $\hat{h}(\vec{x},\omega)$ comprises the contributions of the M_H heat source subsystems $H_i^{(l)}$ contained in Ω_i:

$$\hat{h}(\vec{x},\omega) = -j\omega\,(\gamma - 1) \sum_{l=1}^{M_H} \mathcal{H}_i^{(l)}(\vec{x})\,\hat{Q}_l(\omega) \tag{4}$$

with $\hat{Q}_l(\omega)$ the global fluctuating heat-release of the flame $H_i^{(l)}$, and $\mathcal{H}_i^{(l)}(\vec{x})$ its spatial distribution.

In LOMs based on modal expansion, a volume scalar product is used to perform the Galerkin projection. It is defined as:

$$\langle f, g \rangle = \iiint_{\Omega_i} f(\vec{x}) g(\vec{x})\, d^3\vec{x} \tag{5}$$

A family $(\phi_n(\vec{x}))_{n\geq 1}$ of known acoustic eigenmodes with their associated eigen-pulsations $(\omega_n)_{n\geq 1}$, solutions of the *homogeneous* Helmholtz eigenproblem in Ω_i, is then introduced to seek modal expansions of the acoustic pressure and velocity under the form:

$$\begin{aligned} p(\vec{x},t) &= \sum_{n=1}^{\infty} \dot{\Gamma}_n(t)\phi_n(\vec{x}) = {}^t\dot{\boldsymbol{\Gamma}}(t)\boldsymbol{\phi}(\vec{x}) \\ \vec{u}(\vec{x},t) &= -\frac{1}{\rho_0}\sum_{n=1}^{\infty} \Gamma_n(t)\vec{\nabla}\phi_n(\vec{x}) = -\frac{1}{\rho_0}{}^t\boldsymbol{\Gamma}(t)\vec{\boldsymbol{\nabla}}\boldsymbol{\phi}(\vec{x}) \end{aligned} \tag{6}$$

The family $(\phi_n(\vec{x}))_{n\geq 1}$ is usually chosen as the rigid-wall orthogonal basis that not only verifies $\nabla_s\phi_n = 0$ on S_{wi}, but also on S_{ci}, which makes this expansion unable to satisfy the appropriate condition on the connection boundary. To circumvent this pitfall, a novel type of modal expansion was proposed in [41]: the rigid-wall orthogonal basis is still considered, but it is now *augmented* with the pressure-release orthogonal basis verifying $\phi_n = 0$ on S_{ci}. As the concatenation of two orthogonal bases, $(\phi_n(\vec{x}))_{n\geq 1}$ is not a basis, but is rather an *over-complete frame* [52,53]. The frame projection requires to invert the Gram matrix $\boldsymbol{\Lambda}$ whose coefficients are $\boldsymbol{\Lambda}_{nm} = \langle \phi_n, \phi_m \rangle$. Due to the frame over-completeness, this inversion is a highly ill-conditioned problem, and in practice it is preferable to compute the Moore-Penrose pseudoinverse through a Singular Value Decomposition [54]. For geometrically simple subdomains, the frame can be obtained analytically, whereas for complex subdomains it is generated in a preliminary step thanks to a FEM solver. In addition, the expansion of Eq. (6) is truncated to a finite order N. The frame projection of the Helmholtz equation (Eq. (3)) yields the dynamical system governing the temporal evolution of the modal amplitudes $\Gamma_n(t)$, under the surface forcing from subsystems adjacent to Ω_i, and the volume forcing from heat sources contained within Ω_i:

$$\begin{aligned} \ddot{\Gamma}_n(t) &= -\delta\dot{\Gamma}_n(t) - \omega_n^2\Gamma_n(t) \\ &+ \sum_{m=1}^{M_S} \iint_{S_{ci}^{(m)}} \rho_0 c_0^2 \left(\varphi^{S_{ci}^{(m)}}(\vec{x}_s,t) \left[\boldsymbol{\Lambda}^{-1}\boldsymbol{\nabla_s}\boldsymbol{\phi}(\vec{x}_s)\right]_n - u_s^{S_{ci}^{(m)}}(\vec{x}_s,t) \left[\boldsymbol{\Lambda}^{-1}\boldsymbol{\phi}(\vec{x}_s)\right]_n \right) d^2\vec{x}_s \\ &+ \sum_{l=1}^{M_H} (\gamma-1) Q_l(t) \left[\boldsymbol{\Lambda}^{-1}\langle \boldsymbol{\phi}, \mathcal{H}_i^{(l)} \rangle\right]_n \end{aligned} \tag{7}$$

In this equation (adapted from Eq. (12) in [41]), $\varphi^{S_{ci}^{(m)}}(\vec{x}_s,t)$ and $u_s^{S_{ci}^{(m)}}(\vec{x}_s,t)$ are the acoustic potential and normal velocity in the adjacent complex boundary subsystems $S_{ci}^{(m)}$, respectively. The state-space realization for the volume subdomain Ω_i can be defined from Eq. (7): the resulting state-space matrices are detailed in [41] and are recalled in Supplemental Material B.

2.3. Surface modal expansion for complex boundaries

Let us now consider a complex boundary subsystem $S_{ci}^{(m)}$ that is located at a frontier of the subdomain Ω_i, either connected to another subdomain (*e.g.* $S_{ci}^{(1)}$, $S_{ci}^{(3)}$, $S_{ci}^{(4)}$ in Fig. 1) or to the exterior (*e.g.* $S_{ci}^{(2)}$ in Fig. 1). As previously shown, the potential and velocity in $S_{ci}^{(m)}$ partly govern the acoustics in Ω_i; it is therefore necessary to accurately evaluate the surface integrals in Eq. (7) to enforce the proper subsystem coupling. If the surface area $\Delta S_{ci}^{(m)}$ of the connection boundary $S_{ci}^{(m)}$ is small, such as in the case of a narrow duct giving on a large cavity (*e.g.* $S_{ci}^{(3)}$ in Fig. 1), then the acoustic variables can be considered uniform over the boundary, and the surface integrals in Eq. (7) can be approximated with their value at the center-point $\vec{x}_{sm}$:

$$\iint_{S_{ci}^{(m)}} \rho_0 c_0^2 u_s^{S_{ci}^{(m)}}(\vec{x}_s,t) \left[\boldsymbol{\Lambda}^{-1}\boldsymbol{\phi}(\vec{x}_s)\right]_n d^2\vec{x}_s \approx \rho_0 c_0^2 \Delta S_{ci}^{(m)} u_s^{S_{ci}^{(m)}}(\vec{x}_{sm},t) \left[\boldsymbol{\Lambda}^{-1}\boldsymbol{\phi}(\vec{x}_{sm})\right]_n \tag{8}$$

and similarly for the other surface integral. However, boundaries in realistic combustors often consist of large and geometrically complex, curved panels, and a rough approximation like Eq. (8) is then impracticable. A natural way to overcome this difficulty is to further discretize $S_{ci}^{(m)}$ into smaller surface elements where the acoustic quantities could be considered uniform and the previous approximation would hold, leading to a *piecewise* approximation of the surface integrals. However,

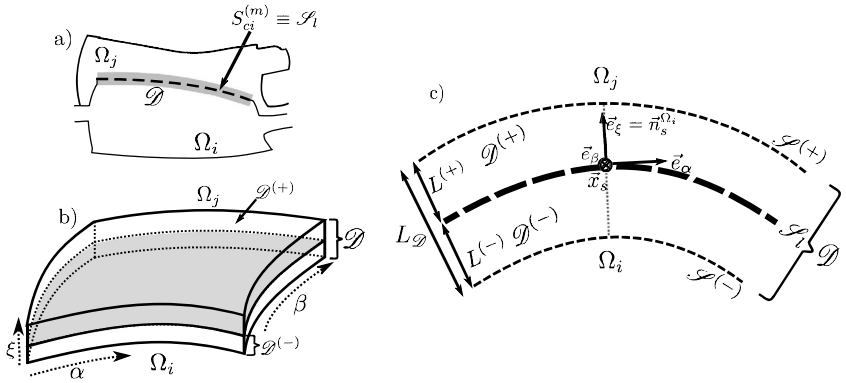

Fig. 2. (a) Schematic of an acoustic network with a complex boundary $S_{ci}^{(m)}$ and a thin control volume $\mathscr{D}$ that encloses it. (b) Three-dimensional representation of the shell-like control volume $\mathscr{D}$ enclosing $\mathscr{S}_l$, and the 2 sub-layers $\mathscr{D}^{(+)}$ and $\mathscr{D}^{(-)}$. (c) Two-dimensional view of $\mathscr{D}$. The sub-layer $\mathscr{D}^{(+)}$ (resp. $\mathscr{D}^{(-)}$) is delimited by the surfaces $\mathscr{S}^{(+)}$ and $\mathscr{S}_l$ (resp. $\mathscr{S}^{(-)}$ and $\mathscr{S}_l$). $\mathscr{D}$ and the 2 sub-layers are parameterized by a common system of coordinates (α, β, ξ), where α and β are curvilinear coordinates tangential to the surface, and ξ is the coordinate normal to the surface. Location of a surface point $\vec{x}_s(\alpha, \beta, \xi = 0)$ is indicated; the associated normal vectors are $\vec{n}_s^{\Omega_i} = +\vec{e}_\xi$ and $\vec{n}_s^{\Omega_j} = -\vec{e}_\xi$.

this approach raises a number of subsequent questions regarding the number, the size, and the locations of the discretized elements necessary to achieve an accurate representation of the surface integrals. Most importantly, even though this spatial discretization may work for a simple Ω_i where the frame $(\phi_n(\vec{x}))_{n\geq 1}$ is obtained analytically, values at the center-points $\vec{x}_{sm}$ are inevitably affected by noise due to numerical approximations when dealing with complex geometries for which frames are numerically assessed (*e.g.* through FEM computations). These minute perturbations can be uncontrollably amplified due to the frame ill-conditioning (in Eq. (7) $\mathbf{\Lambda}^{-1}$ contains very large terms), such that the approximation provided by Eq. (8) is not robust to the details of the numerical procedure used to compute $(\phi_n(\vec{x}))_{n\geq 1}$. In other words, a piecewise approximation of the integrals over $S_{ci}^{(m)}$, combined with the poor conditioning of $\mathbf{\Lambda}$, leads to large and erroneous surface source terms in Eq. (7), which ultimately compromises the entire method. This phenomenon will be more clearly evidenced in Sec. 3.1, where the discretization of an annular liner into 8 smaller surface elements leads to erroneous results, thus calling for a more robust representation of complex-shaped boundaries.

To circumvent this pitfall, we propose to express the surface quantities $u_s^{S_{ci}^{(m)}}(\vec{x}_s, t)$, $\varphi^{S_{ci}^{(m)}}(\vec{x}_s, t)$, $\boldsymbol{\nabla_s \phi}(\vec{x}_s)$, and $\boldsymbol{\phi}(\vec{x}_s)$ appearing in the integrals of Eq. (7) thanks to a *spectral* discretization rather than a spatial one. This spectral discretization is inspired by the Acoustoelastic method [42–44], where acoustic variables in cavities are coupled with thin vibrating membranes: dynamics variables in these membranes are projected on a family of eigenmodes solutions of the Kirchoff-Love equation of shells [55]. The present approach does not rely on this equation, but instead on a curvilinear Helmholtz equation.

Let us illustrate this method in the case of a complex boundary $S_{ci}^{(m)}$ representing a multi-perforated liner between two subdomains Ω_i and Ω_j and characterized by a finite conductivity K_R (but the reasoning also holds for other types of complex boundaries, including those connecting two subdomains without jump conditions, *i.e.* $K_R = \infty$). For conciseness, in this section (and only this one) the boundary $S_{ci}^{(m)}$ is denoted $\mathscr{S}_l$. The aim is to derive a dynamical system analogous to Eq. (7) that governs the acoustics in the vicinity of $\mathscr{S}_l$. In this purpose, a shell-like control volume $\mathscr{D}$ enclosing $\mathscr{S}_l$ is introduced, as shown in Fig. 2. It is split into two distinct sub-layers: $\mathscr{D}^{(-)}$ (resp. $\mathscr{D}^{(+)}$) of thickness $L^{(-)}$ (resp. $L^{(+)}$) located on the side of the subdomain Ω_i (resp. Ω_j). Note that the control volume $\mathscr{D}$ is only an intermediate for the current derivation, such that its thickness $L_{\mathscr{D}}$ does not have any physical meaning and can be chosen arbitrarily small. Once embedded in the LOM network, the entire control volume $\mathscr{D}$ collapses to a two-dimensional manifold corresponding to $\mathscr{S}_l$, or in other words the limit $L_{\mathscr{D}} \to 0$ is retained. This also allows the mean fields c_0 and ρ_0 to be considered uniform within $\mathscr{D}$ along the ξ direction; they can then be defined as the averages of their respective values on $\mathscr{S}^{(-)}$ and $\mathscr{S}^{(+)}$. It will clearly appear later that the values of the mean fields c_0 and ρ_0 in the control volume $\mathscr{D}$ have actually only little importance. The jump relations at the middle surface $\mathscr{S}_l$ relate pressure and flux through:

$$\begin{cases} \hat{u}_\xi^{\mathscr{S}_l^{(-)}}(\alpha, \beta, \omega) = \hat{u}_\xi^{\mathscr{S}_l^{(+)}}(\alpha, \beta, \omega) \\ \left[\hat{p}^{\mathscr{S}_l^{(+)}}(\alpha, \beta, \omega) - \hat{p}^{\mathscr{S}_l^{(-)}}(\alpha, \beta, \omega)\right] = \dfrac{-j\omega d^2 \rho_u}{K_R(j\omega)} \hat{u}_\xi^{\mathscr{S}_l^{(-)}}(\alpha, \beta, \omega) \end{cases} \tag{9}$$

where $\mathscr{S}_l^{(+)}$ (resp. $\mathscr{S}_l^{(-)}$) refers to the values of the variables in $\mathscr{D}^{(+)}$ (resp. $\mathscr{D}^{(-)}$) on the boundary $\mathscr{S}_l$. In Eq. (9) the aperture spacing on the multi-perforated liner is noted d and ρ_u is the upstream mean density. For simplicity, the liner physical parameters are here uniform, but the derivation can be extended to non-uniform cases. It is assumed that the inverse Fourier transform of $-j\omega d^2 \rho_u / K_R(j\omega)$ can be represented by a Single-Input-Single-Output (SISO) state-space real-

ization $\{\mathbf{A_{K_R}}, \mathbf{B_{K_R}}, \mathbf{C_{K_R}}\}$, that relates any input signal $U_{K_R}(t)$ (*e.g.* the velocity) to an output $Y_{K_R}\{U_{K_R}(t)\}$ (*e.g.* the pressure jump across the liner). Such state-space representation exists for any conductivity of the form $K_R(j\omega) = \mathscr{Q}(j\omega)/\mathscr{R}(j\omega)$, where $\mathscr{Q}$ and $\mathscr{R}$ are polynomials. This allows for a great flexibility regarding the conductivity, that can be defined from an analytical model, or fitted to match either experimental or numerical data.

Applying the ξ-averaging $\overline{(.)}^{(-)} = 1/L^{(-)} \int_0^{L^{(-)}} (.) d\xi$ to the linearized Euler equations in the control volume $\mathscr{D}^{(-)}$ yields:

$$\begin{cases} \overline{c_0}^2 \nabla_c^2 \overline{\varphi}^{(-)}(\alpha,\beta,t) - \dfrac{\partial^2 \overline{\varphi}^{(-)}}{\partial t^2}(\alpha,\beta,t) = \dfrac{\overline{c_0}^2}{L^{(-)}} \left[u_\xi^{\Omega_i}(\alpha,\beta,t) - u_\xi^{\mathscr{S}_l^{(-)}}(\alpha,\beta,t) \right] \\ \dfrac{\partial \overline{u}_\xi^{(-)}}{\partial t}(\alpha,\beta,t) = \dfrac{1}{L^{(-)}\overline{\rho_0}} \left[p^{\Omega_i}(\alpha,\beta,t) - p^{\mathscr{S}_l^{(-)}}(\alpha,\beta,t) \right] \end{cases} \tag{10}$$

the first row of which is an inhomogeneous curvilinear Helmholtz equation. In this equation, $u_\xi^{\Omega_i}$ and p^{Ω_i} refer to the values of the variables in Ω_i on the surface $\mathscr{S}^{(-)}$ shown in Fig. 2-(c). The exact expression of the curvilinear Laplacian operator ∇_c^2, as well as the detailed derivation leading to Eq. (10), are provided in Supplemental Material C. Analogous relations are verified in $\mathscr{D}^{(+)}$. The ξ-averaging across the entire control volume $\mathscr{D}$ (excluding the middle surface $\mathscr{S}_l$) is expressed as $\overline{(.)} = (L^{(+)}\overline{(.)}^{(+)} + L^{(-)}\overline{(.)}^{(-)})/L_{\mathscr{D}}$. In addition, the limit $L^{(+)}, L^{(-)} \to 0$ is used to replace $\hat{u}_\xi^{\mathscr{S}_l^{(-)}}$ in the second row of Eq. (9) with the 1st-order approximation $\hat{u}_\xi^{\mathscr{S}_l^{(-)}} \approx \hat{u}_\xi^{\Omega_i}$. Thus, combining Eq. (10), its counterpart for $\mathscr{D}^{(+)}$, and the inverse Fourier transform of Eq. (9) gives:

$$\begin{cases} \overline{c_0}^2 \nabla_c^2 \overline{\varphi}(\alpha,\beta,t) - \dfrac{\partial^2 \overline{\varphi}}{\partial t^2}(\alpha,\beta,t) = \dfrac{\overline{c_0}^2}{L_{\mathscr{D}}} \left[u_\xi^{\Omega_i}(\alpha,\beta,t) - u_\xi^{\Omega_j}(\alpha,\beta,t) \right] \\ \dfrac{\partial \overline{u}_\xi}{\partial t}(\alpha,\beta,t) = \dfrac{1}{L_{\mathscr{D}}\overline{\rho_0}} \left[p^{\Omega_i}(\alpha,\beta,t) - p^{\Omega_j}(\alpha,\beta,t) + Y_{K_R}\left\{ u_\xi^{\Omega_i}(\alpha,\beta,t) \right\} \right] \end{cases} \tag{11}$$

In order to convert Eq. (11) into a state-space representation for the complex boundary $\mathscr{S}_l$, a set of surface modes $(\mathscr{K}_k(\vec{x}_s))_{k\geq 1}$ is introduced. Those are solutions of the following curvilinear Helmholtz eigenproblem in the two-dimensional manifold $\mathscr{S}_l$:

$$\begin{cases} \overline{c_0}^2 \nabla_c^2 \mathscr{K}_k(\alpha,\beta) + \omega_k^2 \mathscr{K}_k(\alpha,\beta) = 0 \text{ in } \mathscr{S}_l \\ \mathscr{K}_k = 0 \text{ or } \vec{\nabla}_c \mathscr{K}_k = 0 \text{ on } \partial\mathscr{S}_l \end{cases} \tag{12}$$

where the curvilinear Laplacian ∇_c^2 and gradient $\vec{\nabla}_c$ are defined in Supplemental Material C. The homogeneous Neumann and Dirichlet conditions on the one-dimensional contour $\partial\mathscr{S}_l$ are chosen to match those of the subdomains Ω_i and Ω_j. It can be demonstrated that $(\mathscr{K}_k(\vec{x}_s))_{k\geq 1}$ is an orthogonal basis of $\mathscr{S}_l$ for the surface scalar product:

$$(f|g) = \iint_{\mathscr{S}_l} f(\vec{x}_s) g(\vec{x}_s)\, d^2\vec{x}_s \tag{13}$$

The squared L-2 norm of the surface modal basis vector $\mathscr{K}_k(\vec{x}_s)$ is noted $\lambda_k = (\mathscr{K}_k|\mathscr{K}_k)$. Similarly to the subdomain frame $(\phi_n)_{n\geq 1}$, the surface modal basis is obtained analytically for a topologically simple surface $\mathscr{S}_l$. For a more complex geometry where an analytical treatment is impossible, $(\mathscr{K}_k)_{k\geq 1}$ can be generated by resolving Eq. (12) thanks to a curvilinear FEM solver. Another possibility, which is the one adopted in this work, consists in building a thin three-dimensional shell domain enclosing $\mathscr{S}_l$, and to resolve the classical homogeneous Helmholtz equation thanks to a 3D FEM solver. Extracting the values on the middle surface then provides good approximations to the solutions of Eq. (12). Note that this shell domain is not related to $\mathscr{D}$, which is only a control volume serving as an intermediate in the derivation of Eq. (11). Surface modal expansions of $\overline{\varphi}$ and $\overline{u}_\xi$ are sought under the form:

$$\begin{aligned} \overline{\varphi}(\alpha,\beta,t) &= \sum_{k=1}^{\infty} \nu_k(t)\mathscr{K}_k(\alpha,\beta) = {}^t\boldsymbol{\nu}(t)\boldsymbol{\mathscr{K}}(\vec{x}_s) \\ \overline{u}_\xi(\alpha,\beta,t) &= \sum_{k=1}^{\infty} \mu_k(t)\mathscr{K}_k(\alpha,\beta) = {}^t\boldsymbol{\mu}(t)\boldsymbol{\mathscr{K}}(\vec{x}_s) \end{aligned} \tag{14}$$

Mimicking the process of the classical Galerkin expansion, Eq. (14) is then injected into Eq. (11), and both the surface scalar product of Eq. (13) and the fact that the orthogonal basis is solution of the curvilinear Helmholtz eigenproblem of Eq. (12) are used. At this point, it is also useful to express the source terms in Eq. (11) thanks to the frame expansions (Eq. (6)) in the subdomains Ω_i and Ω_j to obtain:

$$\begin{cases} \ddot{\nu}_k(t) + \omega_k^2 \nu_k(t) = -\dfrac{\overline{c_0}^2}{\lambda_k L_{\mathscr{D}}} \Bigg[s_i \displaystyle\sum_{n=1}^{N^{(i)}} -\frac{1}{\rho_0^{(i)}} \left(\nabla_s \phi_n^{(i)} | \mathscr{K}_k \right) \Gamma_n^{(i)}(t) \\ \qquad\qquad\qquad\qquad -s_j \displaystyle\sum_{n=1}^{N^{(j)}} -\frac{1}{\rho_0^{(j)}} \left(\nabla_s \phi_n^{(j)} | \mathscr{K}_k \right) \Gamma_n^{(j)}(t) \Bigg] \\ \dot{\mu}_k(t) = \dfrac{1}{\lambda_k L_{\mathscr{D}} \overline{\rho_0}} \Bigg[s_i \displaystyle\sum_{n=1}^{N^{(i)}} \left(\phi_n^{(i)} | \mathscr{K}_k \right) \dot{\Gamma}_n^{(i)}(t) + s_j \sum_{n=1}^{N^{(j)}} \left(\phi_n^{(j)} | \mathscr{K}_k \right) \dot{\Gamma}_n^{(j)}(t) \\ \qquad\qquad + s_i \displaystyle\sum_{n=1}^{N^{(i)}} -\frac{1}{\rho_0^{(i)}} \left(\nabla_s \phi_n^{(i)} | \mathscr{K}_k \right) Y_{K_R} \left\{ \Gamma_n^{(i)}(t) \right\} \Bigg] \end{cases} \tag{15}$$

where the linearity of the operator Y_{K_R} has been used, and where $s_i = \vec{n}_s^{\Omega_i}.\vec{e}_\xi = \pm 1$ and $s_j = \vec{n}_s^{\Omega_j}.\vec{e}_\xi = \mp 1$ define the orientation of the subdomains surface normal vector with respect to the orientation chosen for $\mathscr{D}$. The superscripts $^{(i)}$ and $^{(j)}$ refer to quantities evaluated in Ω_i and Ω_j, respectively. Equation (15) governs the dynamics of the ξ-averaged acoustic potential $\overline{\varphi}$ and normal velocity $\overline{u}_\xi$ in the control volume $\mathscr{D}$, subjected to both the forcing from the adjacent subdomains Ω_i and Ω_j, and to the mechanisms responsible for the complex-valued conductivity K_R. The presence of the time-dependent modal amplitudes $\Gamma_n^{(i)}(t)$ and $\Gamma_n^{(j)}(t)$ in the right-hand side of Eq. (15) shows that the complex boundary $\mathscr{S}_l$ couples the acoustics in Ω_i to that in Ω_j, and *vice versa*. In practice, the control volume $\mathscr{D}$ is not represented once the LOM network is assembled: it instead collapses to the two-dimensional manifold $\mathscr{S}_l$, which allows the thickness $L_{\mathscr{D}}$ to be set to an arbitrarily small value. In the limit $L_{\mathscr{D}} \to 0$, a strong coupling is enforced between Ω_i and Ω_j, as the first row of Eq. (15) enforces the strict flux continuity, while the second row imposes a pressure jump related to K_R. To impose this strong coupling, it is sufficient to choose $L_{\mathscr{D}}$ such that $L_{\mathscr{D}} \ll \min(c_0^{(i)}, c_0^{(j)})/2\pi f_{max}$, where f_{max} is the highest frequency of interest. In the following examples, $L_{\mathscr{D}}$ is fixed to 0.1 mm to satisfy this constrain. Note that in Eq. (15), the surface density $\overline{\rho_0}$ and sound speed $\overline{c_0}$ only appear grouped with the thickness $L_{\mathscr{D}}$, which shows that their specific values have little to no effect on the overall method, as long as $L_{\mathscr{D}}$ is small and that they both remain close to their respective values in Ω_i and Ω_j.

A key aspect of the method lies in the fact that the surface modal expansion of Eq. (14) has to be truncated to a finite order K_S. Determining the optimal size for the surface modal basis, as well as the vectors that are retained to construct it, requires a specific procedure, and an algorithm presented in Appendix C is designed to perform this task.

Finally, the surface modal expansions of Eq. (14) allow the surface integrals in Eq. (7) to be rewritten as:

$$\begin{aligned} &\iint_{S_{ci}^{(m)}} \rho_0 c_0^2 \varphi^{S_{ci}^{(m)}}(\vec{x}_s, t) \left[\boldsymbol{\Lambda}^{-1} \boldsymbol{\nabla_s \phi}(\vec{x}_s) \right]_n d^2\vec{x}_s = \rho_0 c_0^2 \left[\boldsymbol{\Lambda}^{-1} \left(\boldsymbol{\nabla_s \phi} | ^t \mathscr{K} \right) \right]_{n,*} \boldsymbol{\nu}(t) \\ &\iint_{S_{ci}^{(m)}} \rho_0 c_0^2 u_s^{S_{ci}^{(m)}}(\vec{x}_s, t) \left[\boldsymbol{\Lambda}^{-1} \boldsymbol{\phi}(\vec{x}_s) \right]_n d^2\vec{x}_s = s_i \rho_0 c_0^2 \left[\boldsymbol{\Lambda}^{-1} \left(\boldsymbol{\phi} | ^t \mathscr{K} \right) \right]_{n,*} \boldsymbol{\mu}(t) \end{aligned} \tag{16}$$

where $[\ ]_{n,\star}$ denotes the entire n^{th} row of a matrix. The surface source terms in Eq. (7) are now evaluated thanks to the surface modal projections $\left(\boldsymbol{\nabla_s \phi} | ^t \mathscr{K} \right)$ and $\left(\boldsymbol{\phi} | ^t \mathscr{K} \right)$ rather than through simple piecewise approximations as in Eq. (8). This yields a formulation robust with respect to both the frame ill-conditioning and the numerical noise resulting from its construction based on a FEM solver. Equations (15)-(16) show that the original state-space realization for the subdomain Ω_i presented in [41] and Supplemental Material B needs to be adapted. The reformulated state-space matrices are detailed in Appendix A. In addition, these relations are used to define a state-space representation for the acoustics on the complex boundary $S_{ci}^{(m)}$, which is given in Appendix B.

3. Accuracy and convergence assessment

The purpose of this section is twofold: first, it shows the benefit of the surface modal expansion in comparison to the spatial discretization of a boundary; then, it evaluates the precision of the proposed method, through an empirical verification of its convergence on a canonical case with analytically tractable reference solutions. The system of interest, representative of a simplified combustion chamber enclosed in its casing, is shown in Fig. 3. It consists of a cylindrical geometry of radius R_2 and height H, delimited by rigid-walls and comprising an annular ribbon-like acoustic liner of radius R_1 characterized by its Rayleigh conductivity $K_R(j\omega)$. The system is split into an acoustic network of 2 subdomains, and a complex boundary $S_c^{(1)}$ corresponding to the annular liner. In order to be able to satisfy any specified jump relation at this common boundary, modal frames $(\phi_n^{(1)}(\vec{x}))$ and $(\phi_n^{(2)}(\vec{x}))$ are built for each one of the subdomains. They are obtained numerically by using the 3D FEM Helmholtz solver AVSP [9] separately on Ω_1 and Ω_2, which are meshed with uniform

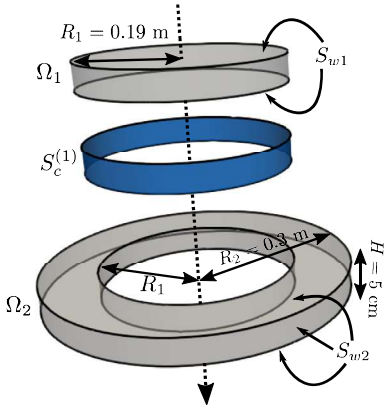

Fig. 3. Exploded view of the acoustic network consisting of 3 subsystems: 2 volume subdomains (an inner cylinder Ω_1 and an outer annulus Ω_2) that share a common connection boundary $S_c^{(1)}$ (in blue). The top, bottom, and external lateral boundaries are rigid-walls. The mean fields are homogeneous within both subdomains, with $c_0 = 347.2$ m/s and $\rho_0 = 1.176$ kg/m^3. (For interpretation of the colors in the figure(s), the reader is referred to the web version of this article.)

tetrahedral cells of dimension $\Delta x = H/10$. Since H is much shorter than other dimensions, longitudinal modes are not included in these frames and will therefore not be discussed in the following. In addition, the number of modes in $(\phi_n^{(1)}(\vec{x}))$ and $(\phi_n^{(2)}(\vec{x}))$ is fixed to a same value $N = N^{(1)} = N^{(2)}$. The surface modal basis $(\mathscr{K}_k(\vec{x}_s))$ of $S_c^{(1)}$ is not computed by directly solving the curvilinear eigenproblem of Eq. (12). The annular ribbon-like strip is instead replaced with a thin 3D annulus where AVSP is used to resolve the classical three-dimensional homogeneous Helmholtz equation. Solutions of Eq. (12) are then obtained by interpolating back the resolved eigenmodes on the two-dimensional manifold $S_c^{(1)}$. A selection algorithm is then applied on this set of curvilinear modes to construct the surface modal basis of $S_c^{(1)}$. As detailed in Appendix C, the algorithm retains only the modes necessary to accurately represent the restriction of the subdomains frames elements on the boundary. The surface modal basis size K_S is therefore a function of the frames size N only. Supplemental Material D details the number and the spatial shapes of the curvilinear modes selected by the construction algorithm; for instance K_S increases from $K_S = 10$ for $N = 20$ to $K_S = 28$ for $N = 100$.

After assembling every state-space representations of the network, the eigenvalues and eigenvectors of the whole system dynamics matrix $\mathbf{A}$ are solved. This yields, for every eigenmode n, its frequency f_n and growth rate σ_n, its pressure spatial distribution $\Upsilon_{p,n}(\vec{x})$, and its velocity distributions $\Upsilon_{u_r,n}(\vec{x})$ and $\Upsilon_{u_\theta,n}(\vec{x})$. In the following, LOM solutions are compared to reference solutions (denoted with a superscript $^{\mathcal{R}}$) thanks to metrics defined for any scalar s or field $g(\vec{x})$:

$$E_s = \frac{|s^{\mathcal{R}} - s|}{s^{\mathcal{R}}} \ , \ \mathcal{E}\{g\}(\vec{x}) = \frac{|g^{\mathcal{R}}(\vec{x}) - g(\vec{x})|}{\max|g^{\mathcal{R}}(\vec{x})|} \tag{17}$$

where E_s is the relative error on the scalar s, and $\mathcal{E}\{g\}$ is the local relative error for $g(\vec{x})$.

3.1. Case of a subdomain simple interface ($K_R = \infty$)

In order to evidence the superiority of the surface modal expansion proposed in Sec. 2.3, in comparison to a piecewise discretization of the annular liner (Eq. (8)), the limit case of an infinitely large conductivity K_R is first inspected. In this situation, the term Y_{K_R} in Eq. (11) and Eq. (15) vanishes, such that at low-frequencies (or equivalently small $L_{\mathscr{D}}$) the acoustics dynamics in $S_c^{(1)}$ reduces to the quasi-static pressure continuity $\left(p^{\Omega_1}|\mathscr{K}\right) = \left(p^{\Omega_2}|\mathscr{K}\right)$ and velocity continuity $\left(u_s^{\Omega_1}|\mathscr{K}\right) = -\left(u_s^{\Omega_2}|\mathscr{K}\right)$ (the negative sign coming from the fact that $\vec{n}_s^{\Omega_1} = -\vec{n}_s^{\Omega_2}$). The liner then behaves as a simple fictive interface between the cylinder and the annulus, and the reference solutions are therefore the eigenmodes of the cylinder of radius R_2 given by:

$$\begin{cases} \Upsilon^{\mathcal{R}}_{p,mn}(r,\theta) = J_n\left(\pi\beta_{mn}\dfrac{r}{R_2}\right)\sin\left(n(\theta-\theta_0)\right) \\ \Upsilon^{\mathcal{R}}_{p,mn}(r,\theta) = J_n\left(\pi\beta_{mn}\dfrac{r}{R_2}\right)\cos\left(n(\theta-\theta_0)\right) \end{cases} , \quad f^{\mathcal{R}}_{mn} = \frac{c_0\beta_{mn}}{2R_2} \tag{18}$$

where J_n is the nth-order Bessel function of the first kind, β_{mn} are the roots of $J_n'(\pi\beta_{mn}) = 0$, and θ_0 is an arbitrary constant.

In this set of computations, the frames size is fixed to $N = 70$, and the surface modal basis contains $K_S(N) = 19$ elements. Fig. 4 compares, for a few selected modes, the results obtained with the surface modal expansion to that coming from a

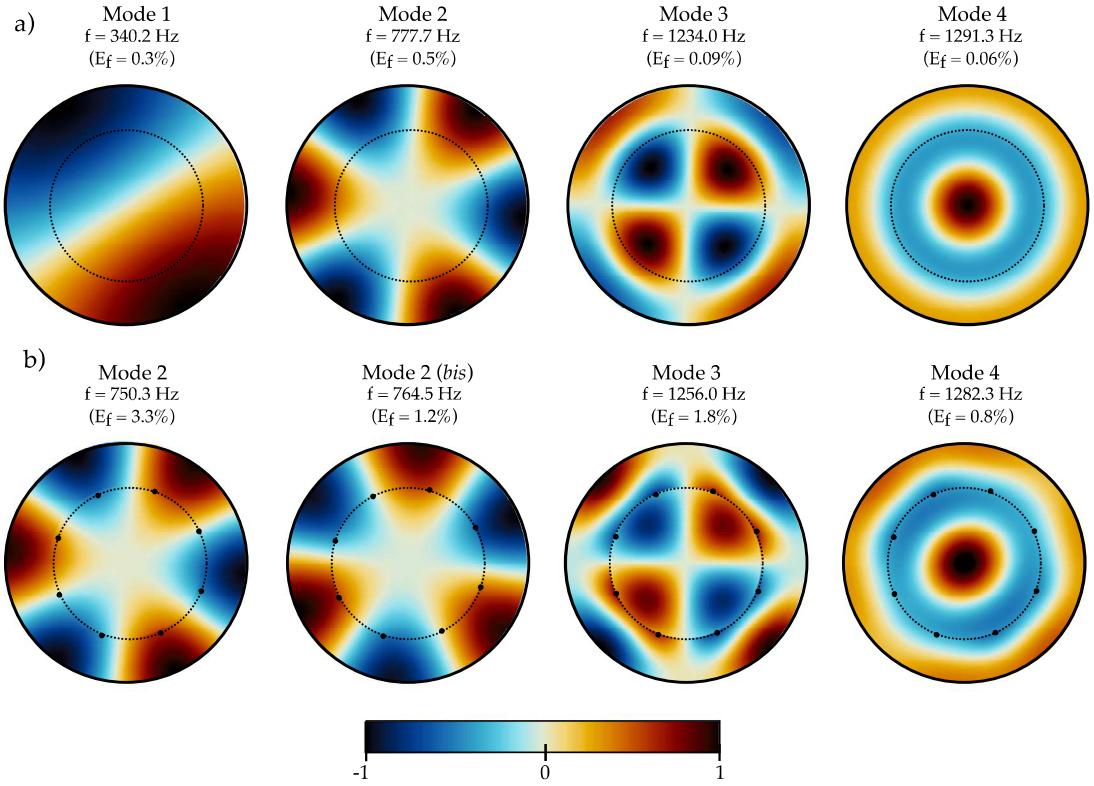

Fig. 4. (a) Pressure distribution $\Upsilon_{p,n}(\vec{x})$ of modes 1 to 4, obtained with a surface modal expansion on the liner. The dashed line represents the location of the connection surface $S_c^{(1)}$ characterized by $K_R = \infty$. (b) Pressure distribution of the modes computed with a spatial discretization of the liner into 8 surface elements. The dark dots indicate the delimitation between these uniformly distributed sub-surfaces. The modal frame size is fixed to $N = 70$ in both cases.

piecewise discretization of the liner into 8 surface elements. Mode 1 is the first azimuthal mode ($n = 0$, $m = 1$, $f_1^{\mathcal{R}} = 339.1$ Hz), mode 2 designates the third azimuthal mode ($n = 0$, $m = 3$, $f_2^{\mathcal{R}} = 773.8$ Hz), mode 3 refers to a mixed radial-azimuthal mode ($n = 1$, $m = 2$, $f_3^{\mathcal{R}} = 1235.2$ Hz), and mode 4 is the second radial mode ($n = 2$, $m = 0$, $f_4^{\mathcal{R}} = 1292.2$ Hz). In the results obtained with the spectral discretization (Fig. 4-(a)), the connection surface $S_c^{(1)}$ does not affect the mode shapes: as expected, it acts as a fictive interface between the two subdomains. In contrast, the spatial discretization of $S_c^{(1)}$ (Fig. 4-(b)) induces a significant distortion of the pressure distribution, most notably for modes 3 and 4. In this case, the continuity of pressure and flux is satisfied at the centers of the 8 discrete surface elements, but not at other points, which leads to discontinuities of the pressure distribution at the interface. The piecewise discretization of $S_c^{(1)}$ not only affects the spatial distribution of the acoustic modes, but it also deteriorates their frequencies. Indeed, the surface modal expansion yields an excellent agreement with the reference frequencies, with relative errors peaking at 0.5 %, whereas those obtained with the surface spatial discretization are one to two orders of magnitude greater. This deterioration is even worse for the third azimuthal mode (modes 2 and 2 *bis* in Fig. 4-(b)), for which two *distinct* frequencies separated by more than 14 Hz correspond to the *same* pressure spatial distribution. Increasing the number of discrete surface elements or the frames size N further deteriorate results yielded by the piecewise discretization. In addition, those were observed to be very sensitive on the locations and respective sizes of the surface elements.

Thus, the piecewise discretization of the annular liner leads to a poor accuracy and to erroneous spatial distributions, even in the trivial case where it should behave as a fictive interface. As explained in Sec. 2.3, this behavior originates from the frame ill-conditioning, which can dramatically amplify numerical approximations stemming from the FEM used to build the frames modes. These highly undesirable features are expected to become even more problematic for complex cases, in which the liner may induce acoustic losses and the subdomains may contain flames, which emphasizes the benefits brought by the surface modal expansion.

3.2. Case of a mutli-perforated liner

The surface modal expansion accuracy and convergence are now evaluated in the more involved situation where the surface $S_c^{(1)}$ is a mutli-perforated acoustic liner. The corresponding Rayleigh conductivity is defined through a generalization of the classical Howe's model [56] accounting for the plate thickness h [57]. However, since the mathematical expression

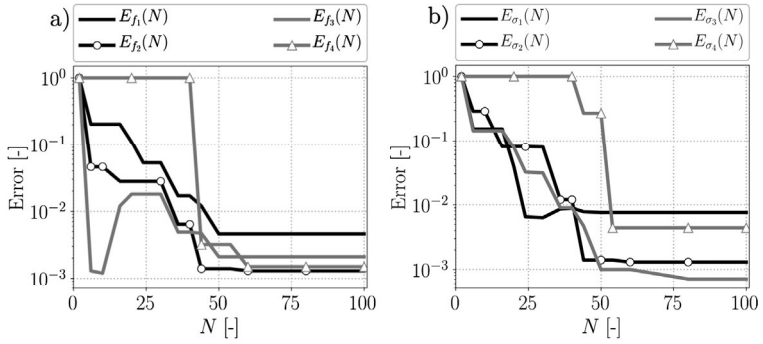

Fig. 5. (a) Frequency relative errors as a function of the modal frame size N, for modes 1 to 4. (b) Growth-rate relative errors in function of N for modes 1 to 4. Errors are plotted with a logarithmic scale.

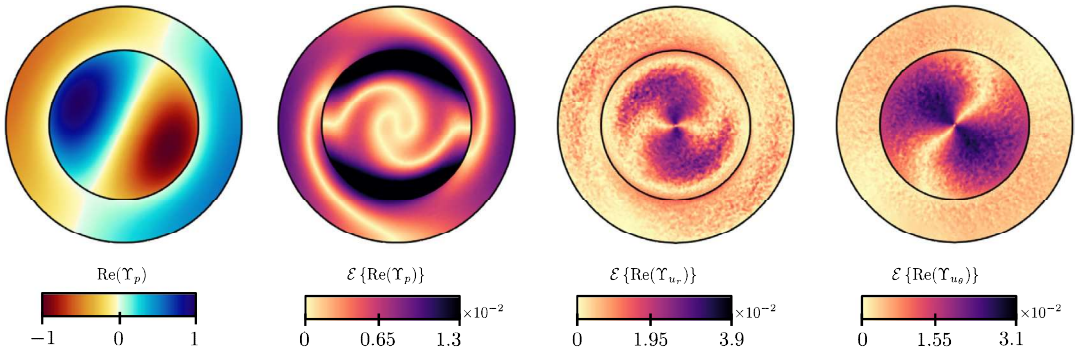

Fig. 6. Comparison between the spatial shape computed with the LOM ($N = 40$) and the reference solution, for the first mixed-mode (mode 3). From left to right: real part of the pressure distribution computed with the LOM, local relative error on the real part of the pressure distribution, local relative error on the real part of the radial velocity distribution, and local relative error on then real part of the azimuthal velocity distribution. All the fields $\Re(\Upsilon_p)(\vec{x})$, $\Re(\Upsilon_{u_r})(\vec{x})$ and, $\Re(\Upsilon_{u_\theta})(\vec{x})$ were normalized beforehand to fit in the range $[-1, 1]$.

of this model comprises complex frequency-dependent Bessel functions, it cannot be directly translated into a state-space realization $\{\mathbf{A_{K_R}}, \mathbf{B_{K_R}}, \mathbf{C_{K_R}}\}$. Instead, the original model is replaced with its 2nd-order polynomial expansion given by:

$$K_R(j\omega) = -K_R^A\, j\omega + K_R^B \omega^2, \text{ with } K_R^A = -\frac{\pi a^2}{2U}\ ,\ K_R^B = \frac{2a^3}{3U^2} + \frac{\pi a^2 h}{4U^2} \tag{19}$$

where a is the aperture radius and U the bias flow speed. This expansion accurately approximates the original model (with discrepancies less than 5%) for $St = a\omega/U \leq 0.3$, a range that encompasses most multi-perforated liners encountered in practical applications. The conductivity state-space realization derived from Eq. (19) is given in Appendix D. The procedure to obtain reference solutions is fully detailed in [14] and recalled in Supplemental Material E.

The Rayleigh conductivity parameters are chosen to induce significant acoustic losses ($a = 0.5$ mm, $d = 5$ mm, $U = 10$ m/s, $h = 1$ mm, $\rho_u = \rho_0$). The LOM convergence is assessed by progressively increasing the number of modes N in the frame expansions, which in turn results in an increase of the surface modal basis size $K_S(N)$. The errors defined in Eq. (17) are then computed in function of N. Low-order results are compared to reference solutions for the first azimuthal mode (mode 1, with $f_1^{\mathcal{R}} = 309.4$ Hz, $\sigma_1^{\mathcal{R}} = -62.6$ s^{-1}), the first radial mode (mode 2, with $f_2^{\mathcal{R}} = 604.4$ Hz, $\sigma_2^{\mathcal{R}} = -372.8$ s^{-1}), the first mixed mode (mode 3, with $f_3^{\mathcal{R}} = 806.8$ Hz, $\sigma_3^{\mathcal{R}} = -257.5$ s^{-1}), and a higher-order 3-3 mixed mode (mode 4, with $f_4^{\mathcal{R}} = 2553$ Hz, $\sigma_4^{\mathcal{R}} = -85$ s^{-1}).

Fig. 5 shows the frequency and growth rates relative errors, as a function of the number of modes N in the frames $(\phi_n^{(1)}(\vec{x}))$ and $(\phi_n^{(2)}(\vec{x}))$. The frequencies and growth rates of modes 1 to 3 rapidly converge towards their respective reference values, as the do not exceed a few percents for N as low as 20. Further increasing N leads to a transitory deterioration for the frequency of mode 3. This behavior is attributed to the frame ill-conditioning, which worsen when its size increases [41, 53]. This deterioration remains however limited and vanishes for $N \geq 30$. Unsurprisingly, the higher-order mode 4 requires a larger frame to be accurately captured. For $N \geq 50$, both the frequencies and growth rates of all the modes considered are accurately resolved with errors ranging from 0.1 % to 0.8 %. Increasing the number of frame modes beyond $N = 80$ does not improve the results, as the minimal achievable error is once again limited by the frames ill-conditioning and by numerical approximations affecting their generation. In Fig. 6 the errors committed by the LOM on the spatial distribution of mode 3 are displayed for a fixed frame size ($N = 40$). The pressure distribution is accurately resolved by the LOM, with a maximum relative error not exceeding 2%. Predictably, the maximum error is reached in the vicinity of the multi-perforated liner where

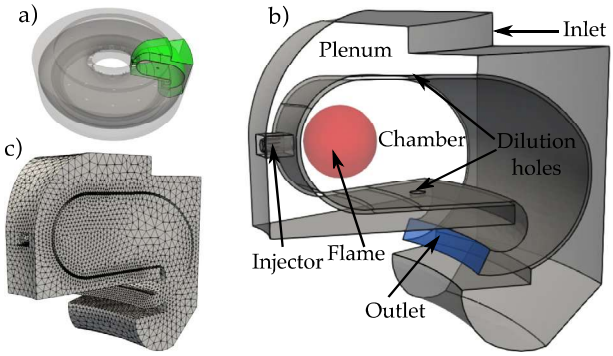

Fig. 7. (a) The annular combustor studied in this section, with one of its 12 sectors highlighted in green. (b) Closeup view of a sector. The red sphere indicates the spatial distribution of heat-release fluctuations, and the blue surface represents the partially reflecting conical outlet of the chamber. (c) Unstructured FEM mesh for one of the sectors. The mesh for the annular configuration, containing 2×10^6 tetrahedral cells, is obtained by rotation and duplication of a single sector mesh. For simplicity, the sound speed and density fields are assumed uniform in the entire domain, with $c_0 = 448.2$ m/s and $\rho_0 = 0.706$ kg/m^3.

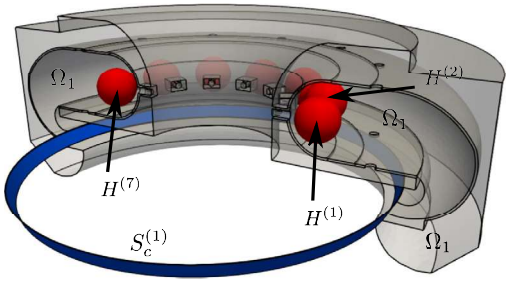

Fig. 8. A 180° view of the acoustic network used in the LOM. The network contains 14 subsystems. The chamber, plenum, injectors, and dilution holes are gathered into a single subdomain Ω_1, which contains 12 heat sources $H^{(l)}$ (in red). It is linked to a complex boundary $S_c^{(1)}$ (in blue) representing the chamber conical outlet, and characterized by an impedance Z. All the other boundaries are rigid-walls.

an important pressure discontinuity occurs. The radial and azimuthal velocity mode shapes are equally well captured, with relative errors locally peaking at 3.9 % and 3.1 %, respectively. Similar trends are displayed for modes 1, 2 and 4, but are not shown here for conciseness. These observations indicate that the combination of the surface and frame modal expansions not only enables the precise resolution of frequencies and growth rates in the presence of significant acoustic losses due to a liner, but also has the ability to capture the pressure and velocity fields, including the large pressure jump through the multi-perforated plate.

4. Application to the partially reflecting outlet of a gas turbine annular combustor

This section aims at assessing the ability of the surface modal expansion method to model complex-shaped impedance boundaries in realistic combustors where thermoacoustic instabilities may exist. The system of interest, represented in Fig. 7, is an annular combustion chamber characteristic of those found in helicopter engine gas turbines. It comprises 12 identical sectors, in each of which a 3 cm radius spherical flame lies 4 cm from the injector exit. The plenum and chamber are linked by dilution holes pierced through the wall. Acoustic losses due to hydrodynamic interactions that may exist at these holes are neglected. The focus is here on the chamber outlet, which may be chocked and be linked to a turbine. It usually cannot be considered as a rigid-wall or a pressure-release boundary, but is rather characterized by a finite impedance Z (or equivalently a reflection coefficient $R = (Z-1)/(Z+1)$). In the seminal work of Marble and Candel [58], a compact chocked outlet has a real-valued impedance $Z = 2/((\gamma-1)M_2)$, with M_2 the Mach number at the outlet. This expression shows that such boundary is only partially reflecting, which may induce acoustic losses and damp the unstable thermoacoustic modes of the combustor. To illustrate the flexibility of the method developed in this paper, in the following the impedance is varied from $Z = +\infty$ (*i.e.* perfectly reflecting rigid-wall, or $R = 1$) to $Z = 1$ (*i.e.* non-reflecting boundary, or $R = 0$).

The low-order acoustic network modeling the annular combustor is shown in Fig. 8. A single subdomain Ω_1 comprising the entire combustor volume is used. It would also be possible to further split Ω_1 into a collection of smaller subdomains (*e.g.* with the plenum, chamber, and injectors as distinct subdomains), but as the aim is here to concentrate on the modeling of the chamber outlet, such decomposition is not necessary. The state-space representation of the outlet boundary is obtained by slightly adapting the dynamical system of Eq. (15) (since here $S_c^{(1)}$ is connected to only one subdomain). The expansion frame of Ω_1, as well as the surface modal basis of $S_c^{(1)}$, are once again generated thanks to the 3D-FEM solver AVSP [9], for which the computational mesh is shown in Fig. 7-(c). Note that the geometry of the complex boundary $S_c^{(1)}$

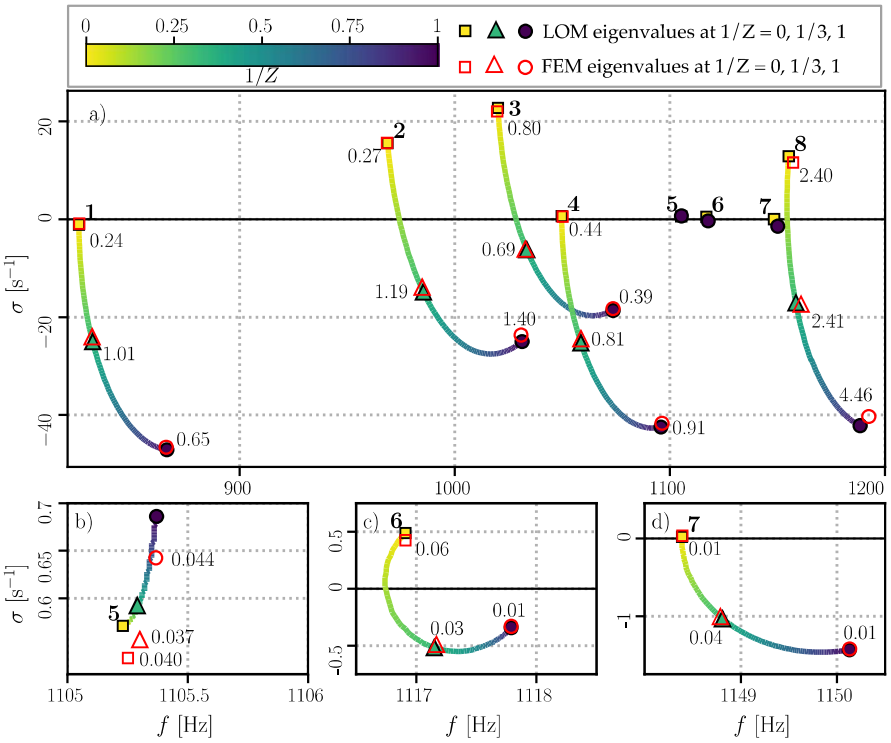

Fig. 9. (a) Trajectories in the complex-frequency plane $f-\sigma$ of the 8 modes computed by the LOM in the range [800 Hz, 1200 Hz], as the outlet impedance is decreased from $Z=+\infty$ to $Z=1$. Dark colored symbols indicate the complex eigenfrequencies computed by the LOM for $Z=+\infty$, $Z=3$, and $Z=1$, while the red symbols show the corresponding FEM reference solutions. The numbers are the absolute errors (in Hz) committed by the LOM at these points. (b), (c), (d) Close-up views on the trajectories of modes 5, 6, and 7, respectively.

differs from that of the liner of Sec. 3 (annular shape), as its radius of curvature is not uniform but depends on the axial coordinate (*conical* shape). The algorithm of Appendix C is used to select the $K_S(N)$ elements that are retained in the construction of the surface modal basis: $K_S(N)$ grows continuously, from $K_S(N=20)=3$ to $K_S(N=240)=17$. More details regarding the surface modal basis elements are given in Supplemental Material D. The response of a given flame $H^{(l)}$ to acoustic fluctuations is modeled by a constant $n-\tau$ FTF:

$$\hat{Q}_l(\omega) = n_f \, e^{-j\omega\tau_f} \, \hat{u}_{f,l}(\vec{x}_{f,l}, \omega) \tag{20}$$

where $n_f = 2000$ J/m is the flame gain, $\tau_f = 1.667$ ms is the time-delay, and $\hat{u}_{f,l}$ is the acoustic velocity at the location $\vec{x}_{f,l}$. This reference point is located at the middle of each one of the 12 injectors. Similarly to previous studies [41,59], the frequency-domain FTF of Eq. (20) is converted into a state-space realization thanks to a Pole Base Function expansion of the time-delay term:

$$e^{-j\omega\tau_f} \approx \sum_{q=1}^{M_P} \frac{-2a_q \, j\omega}{\omega^2 + 2c_q \, j\omega - \omega_{0q}^2} \tag{21}$$

where the coefficients a_q, c_q, ω_{0q} are fitted with a specialized optimization algorithm proposed in [60].

The frequency range of interest spans from 0 Hz to 2000 Hz, and the combustor displays unstable thermoacoustic modes that are all observed to lie between 800 Hz and 1200 Hz. A series of 100 LOM simulations are performed to continuously decrease the outlet impedance from $Z=+\infty$ to $Z=1$. The frame size is fixed to $N=120$, such that the modal surface basis contains $K_S=11$ elements. All 8 modes comprised between 800 Hz and 1200 Hz are computed, and the trajectories they follow in the complex-frequency plane as Z varies are shown in Fig. 9. For validation purpose, the 3D FEM Helmholtz solver AVSP [9] is used to resolve the corresponding reference solutions for a few select impedance values, namely $Z=+\infty$ (perfectly reflecting rigid-wall), $Z=3$ (partially reflecting), and $Z=1$ (anechoic). In addition, the spatial shapes of a few modes at $Z=1$ are compared in Fig. 10. An overall excellent agreement is found between the LOM and the FEM reference solutions for both frequencies, growth rates, and spatial shapes. Modes 1, 2, 3, 4, and 8 are chamber modes and are therefore significantly affected by the decrease of the outlet impedance (Fig. 9-(a)). More particularly, modes 2, 3 and 8 are the most unstable thermoacoustic modes of the combustor for a perfectly reflecting outlet, but decreasing the impedance to $Z=4$ is sufficient to damp and stabilize them. This trend is well captured by the LOM, with errors that do not exceed 5 Hz for

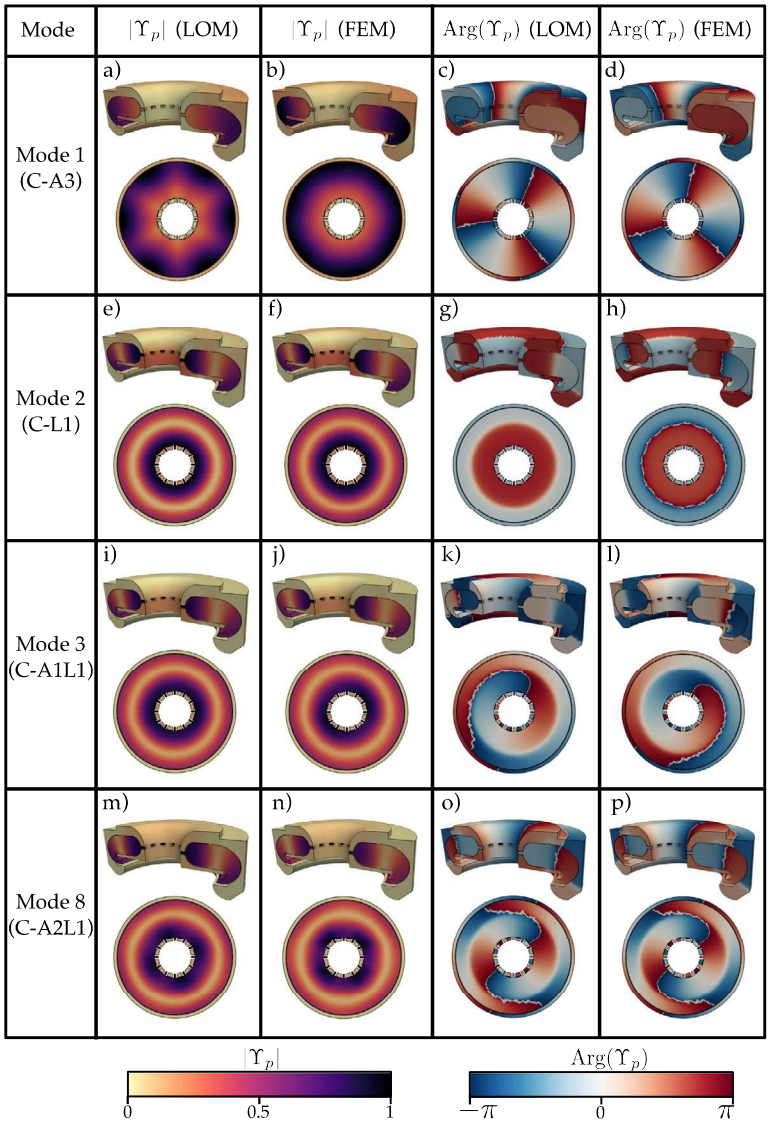

Fig. 10. Pressure mode shape $\Upsilon_p(\vec{x})$ at $Z = 1$ of modes 1, 2, 3, and 8, computed with the LOM and compared to the FEM reference solutions. "C" stands for "Chamber", and AxLy denotes a mode of order x in the azimuthal direction and order y in the longitudinal one. The circular contour plots are on a horizontal plane cutting through the injectors.

mode 8, and stay below 1.5 Hz for the others. Modes 5, 6, and 7 are plenum modes, and the effect of the chamber outlet reflection coefficient on them is therefore more subtle. They remain marginally stable/unstable (*i.e.* with growth rates close to zero), even under anechoic condition. Figs. 9-(b,c,d) evidence the capability of the surface modal expansion method to accurately represent even these minute growth rate and frequency variations. Counterintuitively, a perfectly anechoic outlet does not maximize the damping of modes 2 and 6: their optimal damping is rather reached for a larger reflection coefficient roughly equal to 0.18. This trend is even more remarkable for mode 5 (1st plenum longitudinal mode) as its growth rate steadily increases when R decreases. Such behavior has been observed previous studies [61–63], where the decrease of the reflection coefficient was shown to give rise to unstable thermoacoustic modes, called Intrinsic Thermoacoustic (ITA) instabilities. It is therefore not excluded that modes 2, 5 and 6 are at least partially ITA modes, which does not prevent the proposed approach from accurately resolving them. Only a few minor differences are observed between the LOM spatial mode shapes and the associated FEM reference solutions, most noticeably on the modulus of mode 1 (Fig. 10-(a,b)), which nonetheless vanishes for larger N, and on the phase of mode 3 (Fig. 10-(k,l)). Note, however, that this latter is simply due to the spinning azimuthal component, which can either be clockwise or anticlockwise, and therefore does not indicate an error committed by the LOM.

It is also worth emphasizing the numerical cost associated to the LOM strategy, which leads to the numerical resolution of a *linear* eigenproblem with 860 DoF. In contrast, the 3D FEM approach requires to resolve a *nonlinear* eigenproblem with

2×10^6 DoF. As a result, the 800 LOM modes shown in Fig. 9 were computed in about 10 minutes on a single CPU (in addition to the computational time necessary to numerically construct the subdomain frame and the surface modal basis), whereas the 24 FEM modes displayed for comparison required roughly 5 hours of computation on 72 cores. This confirms the ability of the surface modal expansion method to accurately model the geometrical complexity of realistic outlets in industrial combustors, at a fraction of the cost of a 3D FEM solver.

5. Conclusions

This work introduced a novel method to account for the geometrical complexity of liners and other types of boundaries in the low-order modeling of thermoacoustic instabilities, under the zero Mach number assumption. It essentially combines two methods: (1) the frame modal expansion [41] to model the acoustics in domains comprising boundaries that are neither rigid-walls nor pressure release, and (2) a surface modal expansion reformulated from the acoustoelastic method [42] to model the acoustics in complex-shaped two-dimensional manifolds with non-trivial conductivity or impedance. This latter can be seen as a spectral discretization of the acoustic equations on the topologically complex surface, where the basis elements are solutions of a curvilinear Helmholtz eigenproblem. The approach yields a set of state-space realizations governing the acoustics in the domains, liners, and other boundaries composing the system of interest, which can then be assembled into an acoustic network.

A first example proved the ability of the surface modal expansion to accurately model curved multi-perforated liners typically found in gas-turbine annular combustors. This canonical non-reactive case was also used to assess the expansion convergence: comparison with analytical solutions evidenced a fast convergence of the LOM with respect to both the frame and the surface modal basis sizes. Even though non-monotonic, the error stays bounded within limits yielding highly accurate solutions. In a second example, the conical partially reflecting outlet of an industrial gas turbine combustor comprising flames was modeled with the surface modal expansion. An excellent agreement was observed between the LOM and a FEM Helmholtz solver, with error levels similar to that observed in the previous example. Most importantly, the method proposed was able to account for a wide range of outlet impedance, from perfectly reflecting rigid-wall to purely anechoic. In the end, the surface modal expansion method introduced in this work enables to properly represent the geometrical complexity of boundaries and liners in a LOM framework for thermoacoustics. As such, it may extend the range of applicability of low-order models, from traditional qualitative analysis of idealized systems, to more quantitative modeling of realistic combustors.

CRediT authorship contribution statement

C. Laurent: Methodology Conceptualization, Software implementation, Methodology Validation, Writing: original draft/review/editing

A. Badhe: Methodology Validation, Writing: review

F. Nicoud: Supervision, Methodology Conceptualization, Writing: review and editing, Funding acquisition

Declaration of competing interest

The authors declare that they have no known competing financial interests or personal relationships that could have appeared to influence the work reported in this paper.

Acknowledgements

The first author would like to thank the French Ministry of Higher Education, Research and Innovation and the École Normale Supérieure de Paris-Saclay for funding this work through the CDSN scheme. The second author is grateful for the financial support from the European Union Horizon 2020 research and innovation program under Innovative Training Network (ITN) project ANNULIGhT (grant agreement No 765998).

Appendix A. Reformulation of the state-space realization for a subdomain Ω_i

The state-space representation for the acoustics in a subdomain Ω_i needs to be adapted to account for complex-valued impedance or conductivity on geometrically complex boundaries. For conciseness, Ω_i is assumed to be adjacent to only one complex boundary $S_{ci}^{(m)}$. Since other types of state-space interconnections (simple *point-wise* boundaries, heat sources, etc.) do not require any adaptation, they are not considered here. The reformulated dynamics equation, based on Eq. (7) and Eq. (16), has the following block structure:

$$\underbrace{\frac{d}{dt}\begin{pmatrix}\Gamma_1(t)\\ \dot{\Gamma}_1(t)\\ \vdots\\ \Gamma_N(t)\\ \dot{\Gamma}_N(t)\end{pmatrix}}_{\mathbf{X}^{\Omega_i}(t)} = \underbrace{\begin{pmatrix}0 & 1 & & & \\ -\omega_1^2 & -\delta & & & \\ & & \ddots & & \\ & & & 0 & 1\\ & & & -\omega_N^2 & -\delta\end{pmatrix}}_{\mathbf{A}^{\Omega_i}}\begin{pmatrix}\Gamma_1(t)\\ \dot{\Gamma}_1(t)\\ \vdots\\ \Gamma_N(t)\\ \dot{\Gamma}_N(t)\end{pmatrix} + \underbrace{\begin{pmatrix}\mathbf{B}_{1,1}^{S_{ci}^{(m)}} & \cdots & \mathbf{B}_{1,K_S}^{S_{ci}^{(m)}}\\ \vdots & \ddots & \vdots\\ \mathbf{B}_{N,1}^{S_{ci}^{(m)}} & \cdots & \mathbf{B}_{N,K_S}^{S_{ci}^{(m)}}\end{pmatrix}}_{\mathbf{B}^{\Omega_i}}\underbrace{\begin{pmatrix}\mathbf{U}_1^{S_{ci}^{(m)}}\\ \vdots\\ \mathbf{U}_{K_S}^{S_{ci}^{(m)}}\end{pmatrix}}_{\mathbf{U}^{\Omega_i}(t)} \tag{A.1}$$

where the blocks $\mathbf{B}_{n,k}^{S_{ci}^{(m)}}$ and $\mathbf{U}_k^{S_{ci}^{(m)}}$, used to compute the surface forcing from the complex boundary $S_{ci}^{(m)}$, are given by:

$$\begin{aligned}\mathbf{B}_{n,k}^{S_{ci}^{(m)}} &= \rho_0 c_0^2 \begin{pmatrix} 0 & 0\\ -s_i\left[\mathbf{\Lambda}^{-1}\left(\boldsymbol{\phi}|\mathscr{K}_k^{(m)}\right)\right]_n & \left[\mathbf{\Lambda}^{-1}\left(\boldsymbol{\nabla}_{\boldsymbol{s}}\boldsymbol{\phi}|\mathscr{K}_k^{(m)}\right)\right]_n\end{pmatrix}\\ \mathbf{U}_k^{S_{ci}^{(m)}} &= \frac{1}{\lambda_k}\begin{pmatrix} s_i\left(u_s^{S_{ci}^{(m)}}|\mathscr{K}_k\right)\\ \left(\varphi^{S_{ci}^{(m)}}|\mathscr{K}_k\right)\end{pmatrix} = \begin{pmatrix}\mu_k(t)\\ \nu_k(t)\end{pmatrix}\end{aligned} \tag{A.2}$$

The state vector $\mathbf{X}^{\Omega_i}(t)$ is of size $2N$, with N the number of eigenmodes used in the subdomain frame expansion. The input matrix $\mathbf{B}^{\Omega_i}$ $(2N \times 2K_S)$ serves to compute the surface source terms from the $2K_S$ elements of the input vector $\mathbf{U}^{\Omega_i}$, which comprises the surface modal amplitudes of both the normal velocity and the acoustic potential from the complex boundary $S_{ci}^{(m)}$.

The subsystem Ω_i outputs both the projections of its normal velocity $u_s(\vec{x}_s)$ and pressure $p(\vec{x}_s)$ onto each one of the K_S surface modes of $S_{ci}^{(m)}$. This is achieved thanks to the output equation:

$$\underbrace{\begin{pmatrix}\mathbf{Y}_1^{S_{ci}^{(m)}}\\ \vdots\\ \mathbf{Y}_{K_S}^{S_{ci}^{(m)}}\end{pmatrix}}_{\mathbf{Y}^{\Omega_i}(t)} = \underbrace{\begin{pmatrix}\mathbf{C}_{1,1}^{S_{ci}^{(m)}} & \cdots & \mathbf{C}_{1,N}^{S_{ci}^{(m)}}\\ \vdots & \ddots & \vdots\\ \mathbf{C}_{K_S,1}^{S_{ci}^{(m)}} & \cdots & \mathbf{C}_{K_S,N}^{S_{ci}^{(m)}}\end{pmatrix}}_{\mathbf{C}^{\Omega_i}}\underbrace{\begin{pmatrix}\Gamma_1(t)\\ \dot{\Gamma}_1(t)\\ \vdots\\ \Gamma_N(t)\\ \dot{\Gamma}_N(t)\end{pmatrix}}_{\mathbf{X}^{\Omega_i}(t)} \tag{A.3}$$

where the blocks $\mathbf{C}_{k,n}^{S_{ci}^{(m)}}$ and $\mathbf{Y}_k^{S_{ci}^{(m)}}$ are expressed as:

$$\mathbf{Y}_k^{S_{ci}^{(m)}} = s_i\begin{pmatrix}(u_s|\mathscr{K}_k)\\ (p|\mathscr{K}_k)\end{pmatrix},\ \mathbf{C}_{k,n}^{S_{ci}^{(m)}} = s_i\begin{pmatrix}-\dfrac{1}{\rho_0}(\nabla_s\phi_n|\mathscr{K}_k) & 0\\ 0 & (\phi_n|\mathscr{K}_k)\end{pmatrix} \tag{A.4}$$

Finally, the state-space realization of the subdomain Ω_i with one adjacent complex boundary $S_{ci}^{(m)}$ is a $2K_S$-inputs-$2K_S$-outputs system, whose intrinsic dynamics are governed by a $2N \times 2N$ matrix.

Appendix B. State-space realization for a complex boundary $S_{ci}^{(m)}$

The surface modal amplitudes $\nu_k(t)$ and $\mu_k(t)$ (Eq. (14)) entirely characterize the acoustics dynamics on the complex boundary $S_{ci}^{(m)}$, and are therefore used to build its state-space representation from Eq. (15):

$$\underbrace{\frac{d}{dt}\begin{pmatrix}\mathbf{X}_1^{S_{ci}^{(m)}}\\ \vdots\\ \mathbf{X}_{K_S}^{S_{ci}^{(m)}}\end{pmatrix}}_{\mathbf{X}^{S_{ci}^{(m)}}(t)} = \underbrace{\begin{pmatrix}\mathbf{A}_1^{S_{ci}^{(m)}} & & \\ & \ddots & \\ & & \mathbf{A}_{K_S}^{S_{ci}^{(m)}}\end{pmatrix}}_{\mathbf{A}^{S_{ci}^{(m)}}}\begin{pmatrix}\mathbf{X}_1^{S_{ci}^{(m)}}\\ \vdots\\ \mathbf{X}_{K_S}^{S_{ci}^{(m)}}\end{pmatrix} + \underbrace{\begin{pmatrix}\mathbf{B}_1^{\Omega_{i,j}} & & \\ & \ddots & \\ & & \mathbf{B}_{K_S}^{\Omega_{i,j}}\end{pmatrix}}_{\mathbf{B}^{S_{ci}^{(m)}}}\underbrace{\begin{pmatrix}\mathbf{U}_1^{\Omega_{i,j}}\\ \vdots\\ \mathbf{U}_{K_S}^{\Omega_{i,j}}\end{pmatrix}}_{\mathbf{U}^{S_{ci}^{(m)}}(t)} \tag{B.1}$$

where the blocks $\mathbf{X}_k^{S_{ci}^{(m)}}$, $\mathbf{A}_k^{S_{ci}^{(m)}}$, $\mathbf{B}_k^{\Omega_{i,j}}$, and $\mathbf{U}_k^{\Omega_{i,j}}$ are defined as:

$$\mathbf{X}_k^{S_{ci}^{(m)}} = \begin{pmatrix} \nu_k(t) \\ \dot{\nu}_k(t) \\ \mu_k(t) \\ \mathbf{X}_{\mathbf{K_R},k}(t) \end{pmatrix}, \; \mathbf{A}_k^{S_{ci}^{(m)}} = \begin{pmatrix} 0 & 1 & 0 & \mathbf{0} \\ -\omega_k^2 & 0 & 0 & \mathbf{0} \\ 0 & 0 & 0 & \dfrac{1}{\lambda_k L_{\mathscr{D}} \overline{\rho_0}} \mathbf{C}_{\mathbf{K_R}} \\ 0 & 0 & 0 & \mathbf{A}_{\mathbf{K_R}} \end{pmatrix}$$
$$\mathbf{B}_k^{\Omega_{i,j}} = \begin{pmatrix} 0 & 0 & 0 & 0 \\ -\dfrac{\overline{c_0}^2}{\lambda_k L_{\mathscr{D}}} & 0 & \dfrac{\overline{c_0}^2}{\lambda_k L_{\mathscr{D}}} & 0 \\ 0 & \dfrac{1}{\overline{\rho_0} \lambda_k L_{\mathscr{D}}} & 0 & \dfrac{1}{\overline{\rho_0} \lambda_k L_{\mathscr{D}}} \\ \mathbf{B}_{\mathbf{K_R}} & 0 & 0 & 0 \end{pmatrix}, \mathbf{U}_k^{\Omega_{i,j}} = \begin{pmatrix} s_i\left(u_s^{\Omega_i} | \mathscr{K}_k\right) \\ s_i\left(\varphi^{\Omega_i} | \mathscr{K}_k\right) \\ s_j\left(u_s^{\Omega_j} | \mathscr{K}_k\right) \\ s_j\left(\varphi^{\Omega_j} | \mathscr{K}_k\right) \end{pmatrix} \tag{B.2}$$

In this equation, the subscripts $_{\mathbf{K_R}}$ refer to the SISO state-space realization associated to the inverse Fourier transform of the complex conductivity $K_R(j\omega)$. The blocks $\mathbf{B}_k^{\Omega_{i,j}}$ and $\mathbf{U}_k^{\Omega_{i,j}}$ are employed to compute the source terms from the two adjacent subdomains Ω_i and Ω_j. To be consistent with the subdomains input vectors, $S_{ci}^{(m)}$ must output the modal amplitudes $\nu_k(t)$ and $\mu_k(t)$, which is achieved thanks to:

$$\underbrace{\begin{pmatrix} \mathbf{Y}_1^{\Omega_{i,j}} \\ \vdots \\ \mathbf{Y}_{K_S}^{\Omega_{i,j}} \end{pmatrix}}_{\mathbf{Y}^{S_{ci}^{(m)}}(t)} = \underbrace{\begin{pmatrix} \mathbf{C}_1^{\Omega_{i,j}} & & \\ & \ddots & \\ & & \mathbf{C}_{K_S}^{\Omega_{i,j}} \end{pmatrix}}_{\mathbf{C}^{S_{ci}^{(m)}}} \underbrace{\begin{pmatrix} \mathbf{X}_1^{S_{ci}^{(m)}} \\ \vdots \\ \mathbf{X}_{K_S}^{S_{ci}^{(m)}} \end{pmatrix}}_{\mathbf{X}^{S_{ci}^{(m)}}(t)} \tag{B.3}$$

with:

$$\mathbf{Y}_k^{\Omega_{i,j}} = \begin{pmatrix} \mu_k(t) \\ \nu_k(t) \\ \mu_k(t) \\ \nu_k(t) \end{pmatrix}, \; \mathbf{C}_k^{\Omega_{i,j}} = \begin{pmatrix} 0 & 0 & 1 & \mathbf{0} \\ 1 & 0 & 0 & \mathbf{0} \\ 0 & 0 & 1 & \mathbf{0} \\ 1 & 0 & 0 & \mathbf{0} \end{pmatrix} \tag{B.4}$$

Appendix C. Selection algorithm for constructing the surface modal basis

After obtaining a set $(\mathscr{K}_k)_{k\geq 1}$ solution of the curvilinear Helmholtz eigenproblem of Eq. (12), either through an analytical derivation or a FEM solver, it is necessary to retain a finite number K_S of these modes to build a state-space realization for the boundary $S_{ci}^{(m)}$. As explained in Sec. 2.3, the selection of these modes is driven by the necessity to accurately represent the pressure and the velocity of the subdomain Ω_i on its boundary $S_{ci}^{(m)}$. Since those are computed thanks to the frame modal expansion of Eq. (6), it is in turn crucial to correctly evaluate the frame modes restrictions $\phi_n(\vec{x}_s)$ and their gradients $\nabla_s \phi_n(\vec{x}_s)$ on this surface. Equation (16) and Eq. (15) show that these frame modes restrictions are approximated by their projections on the truncated surface modal basis $(\mathscr{K}_k)_{k\geq 1}$, which write:

$$\boldsymbol{\phi}(\vec{x}_s) \approx \left(\boldsymbol{\phi}|\,{}^t\mathscr{K}\right) \boldsymbol{\lambda}^{-1} \mathscr{K}(\vec{x}_s) \;, \; \boldsymbol{\nabla_s \phi}(\vec{x}_s) \approx \left(\boldsymbol{\nabla_s \phi}|\,{}^t\mathscr{K}\right) \boldsymbol{\lambda}^{-1} \mathscr{K}(\vec{x}_s) \tag{C.1}$$

where $\boldsymbol{\lambda}$ is the diagonal matrix with coefficients $\lambda_k = (\mathscr{K}_k|\mathscr{K}_k)$. The relations in Eq. (C.1) are only approximations because the surface modal basis $(\mathscr{K}_k)_{k\geq 1}$ is truncated up to a finite order K_S, and this truncated set might not be sufficient to *exactly* represent the frame modes and their gradients on the surface. On one hand, a value of K_S too low yields inaccurate projections in Eq. (C.1). On the other hand, including too many surface modes not only results in a more costly LOM because of a large number of DoF, but it can also produce small-amplitude unphysical terms in the matrices $\left(\boldsymbol{\phi}|\,{}^t\mathscr{K}\right)$ and $\left(\boldsymbol{\nabla_s \phi}|\,{}^t\mathscr{K}\right)$, which can in turn be considerably amplified due to the frame ill-conditioning (see the multiplication by $\boldsymbol{\Lambda}^{-1}$ in Eq. (16)). It is therefore of primary importance to appropriately select the size and the modes that are retained in the surface modal basis. In this matter, an algorithm is designed to automatically and robustly construct an optimal surface modal basis $(\mathscr{K}_k)_{k\geq 1}$. It proceeds in 3 steps and is applied in a similar fashion to $\left(\boldsymbol{\phi}|\,{}^t\mathscr{K}\right)$ and to $\left(\boldsymbol{\nabla_s \phi}|\,{}^t\mathscr{K}\right)$:

1. Initially, the surface modal basis $(\mathscr{K}_k)_{k\geq 1}$ is chosen to contain a relatively large number of modes, of which only some will be retained. The SVD of ${}^t\left(\boldsymbol{\phi}|\,{}^t\mathscr{K}\right) \times \left(\boldsymbol{\phi}|\,{}^t\mathscr{K}\right)$ is computed to determine the rank of $\left(\boldsymbol{\phi}|\,{}^t\mathscr{K}\right)$ (since these two matrices have the same rank):

$$ {}^{t}\left(\boldsymbol{\phi}|\,{}^{t}\mathscr{K}\right)\left(\boldsymbol{\phi}|\,{}^{t}\mathscr{K}\right) = \boldsymbol{\mathcal{V}}\,\boldsymbol{\Sigma}\,{}^{t}\boldsymbol{\mathcal{V}} \tag{C.2} $$

The rank r is defined as the number of singular values $\sigma_1, \sigma_2, ..., \sigma_r$ larger than a given threshold $\varepsilon' = \varepsilon_{rk}\sigma_1$. The r corresponding singular vectors $\boldsymbol{\mathcal{V}}_{*,1}, ..., \boldsymbol{\mathcal{V}}_{*,r}$ are isolated.

2. For each singular vector $\boldsymbol{\mathcal{V}}_{*,i}$ $(1 \leq i \leq r)$, its components $\boldsymbol{\mathcal{V}}_{k,i}$ on the surface modes $\mathscr{K}_k$ are sorted in descending order: $|\boldsymbol{\mathcal{V}}_{k1,i}| \geq |\boldsymbol{\mathcal{V}}_{k2,i}| \geq \ldots$. These components are then added one by one until a significant part of the singular vector $\boldsymbol{\mathcal{V}}_{*,i}$ is recovered, or more precisely: $\boldsymbol{\mathcal{V}}^2_{k1,i} + \boldsymbol{\mathcal{V}}^2_{k2,i} + ... + \boldsymbol{\mathcal{V}}^2_{kq,i} \geq (1 - \varepsilon_{sv})|\boldsymbol{\mathcal{V}}_{*,i}|^2$ (q being the smallest integer such that this inequality is verified). The surface modes $\mathscr{K}_{k1}, ..., \mathscr{K}_{kq}$ are therefore the modes that are necessary to represent the singular vector $\boldsymbol{\mathcal{V}}_{*,i}$ and they are added to the list of modes to retain in the surface modal basis. This process is repeated for all the singular vectors $\boldsymbol{\mathcal{V}}_{*,1}, ..., \boldsymbol{\mathcal{V}}_{*,r}$, and the list of surface modes to retain is iteratively incremented.
3. Surface modes that are not included in the list previously computed are discarded and a new surface modal basis is constructed. Note that the K_S modes retained in the surface basis are not necessarily the first K_S eigenmodes solutions of the curvilinear Helmholtz eigenproblem of Eq. (12).

This procedure is systematically applied to construct the surface modal basis. Thus, its size K_S and the modes that it contains are not an input required by the method, but are instead implicitly determined as soon as the subdomains frames are provided. In particular, for a given geometry, the construction of the surface modal basis is independent of the conductivity or impedance value on the boundary, but only depends on the sizes of the adjacent subdomains frames. The thresholds ε_{rk} and ε_{sv} are fixed to $\varepsilon_{rk} = 10^{-2}$ and $\varepsilon_{sv} = 0.2$. They do not require to be tuned for the examples presented in this paper.

Appendix D. State-space realization of a Rayleigh conductivity K_R

For a Rayleigh conductivity K_R expressed through the approximation to Howe's model given in Eq. (19), the inverse Fourier transform of the term $-j\omega\rho_u d^2/K_R(j\omega)$ in Eq. (9) can be translated into a SISO state-space realization that is directly embedded into the complex boundary state-space realization provided in Eq. (B.1)-(B.2). Its expression writes:

$$ \underbrace{\frac{\mathrm{d}}{\mathrm{d}t}\left(z(t)\right)}_{\mathbf{x}_{\mathbf{K_R}}(t)} = \underbrace{\left(-K_R^A/K_R^B\right)}_{\mathbf{A}_{\mathbf{K_R}}}\left(z(t)\right) + \underbrace{\left(-1/K_R^B\right)}_{\mathbf{B}_{\mathbf{K_R}}}\left(s_i\left(u_s^{\Omega_i}|\mathscr{K}_k\right)\right) \tag{D.1} $$

and the output Y_{K_R} is computed through:

$$ \left(Y_{K_R}(t)\right) = \underbrace{\left(-\rho_u d^2\right)}_{\mathbf{C}_{\mathbf{K_R}}}\left(z(t)\right) \tag{D.2} $$

Appendix E. Supplementary material

Supplementary material related to this article can be found online

References

[1] T. Poinsot, Prediction and control of combustion instabilities in real engines, Proc. Combust. Inst. 36 (1) (2017) 1–28.
[2] D.T. Harrje, Liquid propellant rocket combustion instability, NASA-SP-194.
[3] J.C. Oefelein, V. Yang, Comprehensive review of liquid-propellant combustion instabilities in F-1 engines, J. Propuls. Power 9 (5) (1993) 657–677.
[4] J.L. Rayleigh, The explanation of certain acoustical phenomena, Nature 18 (1878) 319–321.
[5] J.-F. Bourgouin, D. Durox, J.P. Moeck, T. Schuller, S. Candel, Characterization and modeling of a spinning thermoacoustic instability in an annular combustor equipped with multiple matrix injectors, J. Eng. Gas Turbines Power 137 (2) (2015) 021503.
[6] A. Urbano, L. Selle, G. Staffelbach, B. Cuenot, T. Schmitt, S. Ducruix, S. Candel, Exploration of combustion instability triggering using Large Eddy Simulation of a multiple injector Liquid Rocket Engine, Combust. Flame 169 (2016) 129–140.
[7] P. Wolf, R. Balakrishnan, G. Staffelbach, L.Y. Gicquel, T. Poinsot, Using LES to study reacting flows and instabilities in annular combustion chambers, Flow Turbul. Combust. 88 (1–2) (2012) 191–206.
[8] L. Crocco, Aspects of combustion stability in liquid propellant rocket motors part i: fundamentals. Low frequency instability with monopropellants, J. Am. Rocket Soc. 21 (6) (1951) 163–178.
[9] F. Nicoud, L. Benoit, C. Sensiau, T. Poinsot, Acoustic modes in combustors with complex impedances and multidimensional active flames, AIAA J. 45 (2) (2007) 426–441.
[10] S. Camporeale, B. Fortunato, G. Campa, A finite element method for three-dimensional analysis of thermo-acoustic combustion instability, J. Eng. Gas Turbines Power 133 (1) (2011) 011506.
[11] D. Laera, T. Schuller, K. Prieur, D. Durox, S.M. Camporeale, S. Candel, Flame describing function analysis of spinning and standing modes in an annular combustor and comparison with experiments, Combust. Flame 184 (2017) 136–152.
[12] G.A. Mensah, G. Campa, J.P. Moeck, Efficient computation of thermoacoustic modes in industrial annular combustion chambers based on bloch-wave theory, J. Eng. Gas Turbines Power 138 (8) (2016) 081502.
[13] W. Krebs, G. Walz, P. Flohr, S. Hoffmann, Modal analysis of annular combustors: effect of burner impedance, in: ASME Turbo Expo 2001: Power for Land, Sea, and Air, American Society of Mechanical Engineers Digital Collection, 2001.
[14] E. Gullaud, F. Nicoud, Effect of perforated plates on the acoustics of annular combustors, AIAA J. 50 (12) (2012) 2629–2642.

[15] A. Andreini, C. Bianchini, B. Facchini, F. Simonetti, A. Peschiulli, Assessment of numerical tools for the evaluation of the acoustic impedance of multi-perforated plates, in: ASME 2011 Turbo Expo: Turbine Technical Conference and Exposition, American Society of Mechanical Engineers Digital Collection, 2011, pp. 1065–1077.
[16] A. Giusti, A. Andreini, B. Facchini, I. Vitale, F. Turrini, Thermoacoustic analysis of a full annular aero-engine lean combustor with multi-perforated liners, in: 19th AIAA/CEAS Aeroacoustics Conference, 2013, p. 2099.
[17] F. Ni, F. Nicoud, Y. Méry, G. Staffelbach, Including flow–acoustic interactions in the helmholtz computations of industrial combustors, AIAA J. (2018) 1–15.
[18] M. Bauerheim, A. Ndiaye, P. Constantine, S. Moreau, F. Nicoud, Symmetry breaking of azimuthal thermoacoustic modes: the UQ perspective, J. Fluid Mech. 789 (2016) 534–566.
[19] M. Bauerheim, J.F. Parmentier, P. Salas, F. Nicoud, T. Poinsot, An analytical model for azimuthal thermoacoustic modes in an annular chamber fed by an annular plenum, Combust. Flame 161 (5) (2014) 1374–1389.
[20] T. Emmert, M. Meindl, S. Jaensch, W. Polifke, Linear state space interconnect modeling of acoustic systems, Acta Acust. Acust. 102 (5) (2016) 824–833.
[21] M. Meindl, A. Albayrak, W. Polifke, A state-space formulation of a discontinuous Galerkin method for thermoacoustic stability analysis, J. Sound Vib. (2020) 115431.
[22] S.R. Stow, A.P. Dowling, Thermoacoustic oscillations in an annular combustor, in: ASME Turbo Expo 2001: Power for Land, Sea, and Air, American Society of Mechanical Engineers Digital Collection, 2001.
[23] A.P. Dowling, S.R. Stow, Acoustic analysis of gas turbine combustors, J. Propuls. Power 19 (5) (2003) 751–764.
[24] J. Li, D. Yang, C. Luzzato, A. Morgans, OSCILOS: the open source combustion instability low order simulator, Tech. Rep., Imperial, College London, 2014, http://www.oscilos.com.
[25] Y. Xia, D. Laera, A.S. Morgans, W. Jones, J.W. Rogerson, Thermoacoustic limit cycle predictions of a pressurised longitudinal industrial gas turbine combustor, in: ASME Turbo Expo 2018: Turbomachinery Technical Conference and Exposition, American Society of Mechanical Engineers Digital Collection, 2018.
[26] D. Yang, A.S. Morgans, Low-order network modeling for annular combustors exhibiting longitudinal and circumferential modes, in: ASME Turbo Expo 2018: Turbomachinery Technical Conference and Exposition, American Society of Mechanical Engineers Digital Collection, 2018.
[27] S. Akamatsu, A. Dowling, Three dimensional thermoacoustic oscillation in a premix combustor, in: ASME Turbo Expo 2001: Power for Land, Sea, and Air, American Society of Mechanical Engineers Digital Collection, 2001.
[28] M. Namba, K. Fukushige, Application of the equivalent surface source method to the acoustics of duct systems with non-uniform wall impedance, J. Sound Vib. 73 (1) (1980) 125–146.
[29] X. Sun, X. Wang, L. Du, X. Jing, A new model for the prediction of turbofan noise with the effect of locally and non-locally reacting liners, J. Sound Vib. 316 (1–5) (2008) 50–68.
[30] G. Zhang, X. Wang, L. Li, X. Jing, X. Sun, Control of thermoacoustic instability with a drum-like silencer, J. Sound Vib. 406 (2017) 253–276.
[31] A. Cardenas-Miranda, W. Polifke, Combustion stability analysis of rocket engines with resonators based on Nyquist plots, J. Propuls. Power 30 (4) (2014) 962–977.
[32] G. Gabard, R. Astley, A computational mode-matching approach for sound propagation in three-dimensional ducts with flow, J. Sound Vib. 315 (4–5) (2008) 1103–1124.
[33] G. Zhang, X. Wang, L. Li, X. Sun, Effects of perforated liners on controlling combustion instabilities in annular combustors, AIAA J. (2020) 1–15.
[34] S. Bethke, U. Wever, W. Krebs, Stability analysis of gas-turbine combustion chamber, in: 11th AIAA/CEAS Aeroacoustics Conference, 2005, p. 2831.
[35] P.M. Morse, K.U. Ingard, Theoretical Acoustics, Princeton University Press, 1968.
[36] F. Culick, Nonlinear behavior of acoustic waves in combustion chambers—ii, Acta Astronaut. 3 (9–10) (1976) 735–757.
[37] F. Culick, Combustion instabilities in liquid-fuelled propulsion systems.
[38] F.E. Culick, V. Yang, Overview of combustion instabilities in liquid-propellant rocket engines, in: Liquid Rocket Engine Combustion Instability, vol. 169, 1995, pp. 3–37.
[39] F. Culick, Unsteady motions in combustion chambers for propulsion systems, NATO Research and Technonoly Organization No. AC/323 (AVT-039) TP/10.
[40] G. Ghirardo, F. Boudy, M.R. Bothien, Amplitude statistics prediction in thermoacoustics, J. Fluid Mech. 844 (2018) 216–246.
[41] C. Laurent, M. Bauerheim, T. Poinsot, F. Nicoud, A novel modal expansion method for low-order modeling of thermoacoustic instabilities in complex geometries, Combust. Flame 206 (2019) 334–348.
[42] E.H. Dowell, G. Gorman, D. Smith, Acoustoelasticity: general theory, acoustic natural modes and forced response to sinusoidal excitation, including comparisons with experiment, J. Sound Vib. 52 (4) (1977) 519–542.
[43] B. Laulagnet, J.L. Guyader, Modal analysis of a shell's acoustic radiation in light and heavy fluids, J. Sound Vib. 131 (3) (1989) 397–415.
[44] J. Missaoui, L. Cheng, A combined integro-modal approach for predicting acoustic properties of irregular-shaped cavities, J. Acoust. Soc. Am. 101 (6) (1997) 3313–3321.
[45] S.R. Stow, A.P. Dowling, A time-domain network model for nonlinear thermoacoustic oscillations, J. Eng. Gas Turbines Power 131 (3) (2009) 031502.
[46] B. Schuermans, V. Bellucci, C.O. Paschereit, Thermoacoustic modeling and control of multi burner combustion systems, in: ASME Turbo Expo 2003, Collocated with the 2003 International Joint Power Generation Conference, American Society of Mechanical Engineers, 2003, pp. 509–519.
[47] B. Schuermans, Modeling and control of thermoacoustic instabilities, Ph.D. thesis, EPFL, 2003.
[48] N. Noiray, B. Schuermans, Theoretical and experimental investigations on damper performance for suppression of thermoacoustic oscillations, J. Sound Vib. 331 (12) (2012) 2753–2763.
[49] V. Bellucci, B. Schuermans, D. Nowak, P. Flohr, C.O. Paschereit, Thermoacoustic modeling of a gas turbine combustor equipped with acoustic dampers, in: ASME Turbo Expo 2004: Power for Land, Sea, and Air, American Society of Mechanical Engineers, 2004, pp. 635–644.
[50] D. Yang, F.M. Sogaro, A.S. Morgans, P.J. Schmid, Optimising the acoustic damping of multiple Helmholtz resonators attached to a thin annular duct, J. Sound Vib. 444 (2019) 69–84.
[51] R. Redheffer, On a certain linear fractional transformation, Stud. Appl. Math. 39 (1–4) (1960) 269–286.
[52] I. Daubechies, A. Grossmann, Y. Meyer, Painless nonorthogonal expansions, J. Math. Phys. 27 (5) (1986) 1271–1283.
[53] B. Adcock, D. Huybrechs, Frames and numerical approximation, SIAM Rev. 61 (3) (2019) 443–473.
[54] G. Golub, W. Kahan, Calculating the singular values and pseudo-inverse of a matrix, J. Soc. Ind. Appl. Math., Ser. B Numer. Anal. 2 (2) (1965) 205–224.
[55] S.P. Timoshenko, S. Woinowsky-Krieger, Theory of Plates and Shells, McGraw-Hill, 1959.
[56] M. Howe, On the theory of unsteady high reynolds number flow through a circular aperture, Proc. R. Soc. Lond. Ser. A, Math. Phys. Sci. 366 (1725) (1979) 205–223.
[57] X. Sun, X. Jing, H. Zhang, Y. Shi, Effect of grazing–bias flow interaction on acoustic impedance of perforated plates, J. Sound Vib. 254 (3) (2002) 557–573.
[58] F. Marble, S. Candel, Acoustic disturbance from gas non-uniformities convected through a nozzle, J. Sound Vib. 55 (2) (1977) 225–243.
[59] G. Ghirardo, B. Ćosić, M.P. Juniper, J.P. Moeck, State-space realization of a describing function, Nonlinear Dyn. 82 (1–2) (2015) 9–28.
[60] Q. Douasbin, C. Scalo, L. Selle, T. Poinsot, Delayed-time domain impedance boundary conditions (D-TDIBC), J. Comput. Phys. 371 (2018) 50–66.
[61] C.F. Silva, M. Merk, T. Komarek, W. Polifke, The contribution of intrinsic thermoacoustic feedback to combustion noise and resonances of a confined turbulent premixed flame, Combust. Flame 182 (2017) 269–278.

[62] T. Emmert, S. Bomberg, S. Jaensch, W. Polifke, Acoustic and intrinsic thermoacoustic modes of a premixed combustor, Proc. Combust. Inst. 36 (3) (2017) 3835–3842.
[63] L. Xu, J. Zheng, G. Wang, Z. Feng, X. Tian, L. Li, F. Qi, Investigation on the intrinsic thermoacoustic instability of a lean-premixed swirl combustor with an acoustic liner, Proc. Combust. Inst. (2020), https://doi.org/10.1016/j.proci.2020.06.155.